**Figure 3 | Microdistribution of fluorescently labelled DACHPt/m of varying sizes in tumours. a–d,** Histological examination of C26 tumour (**a**) and BxPC3 tumour (**c**) by H&E staining (dashed lines in **c** show area of cancer cell nests in the BxPC3 tumour) and fluorescent microscopic images of sections of C26 (**b**) and BxPC3 (**d**) tumours 24 h after intravenous administration of fluorescent micelles with different sizes. Micelles were labelled with Alexa 594 (red). Blood vessels were marked with PECAM-1 and Alexa 488 secondary antibody (green). Scale bars, 50 μm. **e–g,** Mapping of platinum atoms from DACHPt and iron from haemoproteins in tumour sections of C26 (**e**), BxPC3 (**f**) and a BxPC3 cancer cell nest (indicated by dashed line) (**g**) by μ-SR-XRF 24 h after administration of micelles. Scale bars, 50 μm.

against the penetration of drugs and nanocarriers[20,31]. In the BxPC3 model, immunofluorescence detection of PECAM-1 (Fig. 3d, green) indicated the presence of blood vessels around the cancer cell nests and the absence of vessels in the interior of these structures. We observed that the 30 nm micelles penetrated inside the tightly nested structures of BxPC3 tumours, but the fluorescent signal of the bigger micelles diminished and was concentrated close to the blood vessels, indicating their failure to enter the nests of cancer cells (Fig. 3d, red). This size-dependent penetration of fluorescent

DACHPt/m may affect the intratumoral distribution of the delivered drug.

Given that the drug loaded in the micelles was a platinum complex, we assessed the drug microdistribution in tumour sections by detecting element disposition using μ-synchrotron radiation X-ray fluorescence (μ-SR-XRF). The very distinct peak of the platinum from the DACHPt can be observed in the sum spectrum of the line scan as well as the elements traditionally present in animal tissue. The distribution of iron and platinum in tumour tissue

sections was studied to evaluate the distribution of haemoproteins (linked to the presence of blood vessels) and the location of the drug, respectively. For this experiment, we used DACHPt/m with diameters of 30 and 70 nm because of the critical differences in antitumour activity, tumour accumulation and microdistribution of DACHPt/m in the BxPC3 tumour model for diameters below and above 50 nm (Figs 2c,d, 3d).

In the C26 tumour model, the extensive spread of iron atoms indicates abundant vascularization (Fig. 3e), consistent with the abundance of blood vessels observed by immunofluorescence microscopy (Fig. 3b, green). DACHPt delivered from the 30 and 70 nm micelles was broadly distributed in this tumour model (Fig. 3e). In the BxPC3 xenografts, the distribution of iron atoms (Fig. 3f,g) indicates reduced vascularization and disposition of blood vessels in this model, suggesting a restricted blood flow inside the nest structures. The platinum mapping shows that the 30 nm micelles delivered DACHPt inside the cancer cell nests, whereas DACHPt from the 70 nm micelles is localized in the periphery of the nests (Fig. 3g). In both tumour models, the intratumoral microdistribution of DACHPt has a layout similar to that of the fluorescent micelles, confirming that tumour penetration by the micelles directly affects drug accumulation and antitumour outcome.

The real-time observation of in vivo behaviour of nanocarriers might reveal the critical barriers in a living body. Unlike conventional histological analysis, the in vivo confocal laser scanning microscopy (CLSM) technique enables spatiotemporal and quantitative analyses of extravasation, tissue penetration and cellular internalization of nanocarriers in a living animal[34]. By using an in vivo CLSM combined with a high-speed resonance scanner designed to acquire clean live tissue images, we intravitally evaluated the penetration and accumulation of the fluorescently labelled micelles. The 30 and 70 nm micelles were labelled with Alexa 488 (green) and Alexa 594 (red) fluorescent probes, respectively (Supplementary Fig. S3), and concurrently injected into tumour-bearing mice to evaluate real-time extravasation, penetration and microdistribution of both micelles in the same tumour (Fig. 4). Fluorescence measurements in the tissues were relative to the fluorescence intensity in the vasculature immediately after injection of the micelles ($V_{max}$).

At 1 h post-injection of the micelles, the fluorescence intensity of both 30 and 70 nm DACHPt/m in the blood vessels of tumours was ~80% of $V_{max}$ (Fig. 4a,b). In C26 tumours, the micelles showed similar extravasation and penetration (Fig. 4a, Supplementary Video S1). The z-stack volume reconstruction of the C26 tumour showed a profusely vascularized structure and a comparable presence of both micelles in the tumour interstitium (Fig. 4c, Supplementary Video S2). In BxPC3 tumours, the extravasation profiles of the 30 and 70 nm micelles after 1 h were clearly dissimilar (Fig. 4b, Supplementary Videos S3, S4). The 30 nm micelles crossed the vascular wall, achieving over 20% of $V_{max}$ at 40 μm from the blood vessel (Fig. 4b). In contrast, the 70 nm micelles extravasated at discrete sites close to the blood vessels and failed to move towards the interstitial space (Fig. 4b). These distinct penetration profiles were evident in the z-stack volume reconstruction of the BxPC3 tumour, showing that the extravasation points of the 70 nm micelles surrounded the blood vessels (Fig. 4d,e, Supplementary Videos S5 and S6). At 24 h post-injection, the intensities of the extravasated 30 and 70 nm micelles in the C26 tumour were ~40% of $V_{max}$ at 100 μm from the blood vessels (Fig. 4f), and both micelles were observed inside the individual cells of the tumour tissue (Fig. 4f). In BxPC3 tumours, the distribution of the micelles corresponded reasonably to their different extravasation profiles; the 30 nm micelles achieved deep tumour accumulation, but the 70 nm micelles remained close to the vasculature (Fig. 4g, white arrows). The intensity of the extravasated 30 nm micelles was ~40% of $V_{max}$ (Fig. 4g) and they apparently localized in the cells (Fig. 4g). These observations strongly suggest that

30 nm DACHPt/m can penetrate nests of cancer cells distant from blood vessels, allowing homogeneous drug distribution in hypopermeable tumours.

Although many factors (including morphology, hydrophobicity and nanoparticle charge) affect their accumulation in tumours, it is of primary importance to study long-circulating nanocarriers, because prolonged circulation is a prerequisite for tumour targeting based on the EPR effect. Results obtained by intratumoral microdistribution studies indicate that micellar nanomedicines with diameters less than 50 nm might be superior in terms of extravasation and penetration into tumour tissues among the sub-100 nm micellar nanomedicines. The limitation of the present study is that the size of the micellar nanomedicines was restricted to between 30 and 100 nm. Because the threshold of renal clearance of nanoparticles is ~5.5 nm (ref. 35), tumour accumulation and intratumoral distribution of nanomedicines in the range between 5 and 30 nm remain to be clarified. Furthermore, the biodistribution study revealed that the 100 nm micelles showed higher accumulation in the liver compared with other smaller micelles (Supplementary Fig. S2, Table S1), suggesting the importance of the size of nanomedicines for their distribution in organs, which may be associated with toxicity. Hence, optimizing the size of nanomedicines should take into account the balance between antitumour efficacy and potential toxicity.

## Enhancing tumour permeability with a TGF-β inhibitor

We have recently reported that low doses of a transforming growth factor (TGF)-β inhibitor (TGF-β-I) transiently decreases the pericyte coverage of the endothelium in the neovasculature of pancreatic tumours, resulting in enhanced accumulation and antitumour activity of 65 nm micellar nanomedicines and 90 nm Doxil[20]. These results motivated us to evaluate the effect of the TGF-β inhibitor on the delivery of sub-100 nm DACHPt/m in BxPC3 tumours. When mice were treated with 1 mg kg$^{-1}$ of TGF-β-I (LY364947), the 70 nm micelles reduced the tumour growth rate as effectively as the 30 nm micelles (Fig. 5a). Moreover, accumulation of the 70 nm micelles in tumours was augmented to a level comparable with that of the 30 nm micelles (Fig. 5b). These results indicate that the impaired extravasation and penetration of the 70 nm micelles in BxPC3 tumours can be overcome by treatment with TGF-β-I.

Fluorescence microscopic evaluation of BxPC3 tumour sections revealed that the fluorescently labelled 70 nm micelles showed enhanced intratumoural penetration even inside cancer cell nests after administration of TGF-β-I (Fig. 5c). This result suggests that modulation of the stromal components in tumour tissue by TGF-β-I, including pericyte coverage around the tumour blood vessels, is important for penetration of the 70 nm micelles. Moreover, the μ-SR-XRF measurement demonstrated that co-administration of TGF-β-I facilitated intratumoral delivery of DACHPt from the 70 nm micelles, which reached the interior of the cancer cell nests at 24 h post-injection (Fig. 5d). This result is consistent with the augmented antitumour activity (Fig. 5a) and enhanced intratumoural penetration (Fig. 5b) of 70 nm DACHPt/m by TGF-β-I.

Intravital CLSM observation also confirmed that treatment with TGF-β-I enhanced the extravasation and penetration of 70 nm micelles into BxPC3 tumours (Fig. 5e, Supplementary Video S7). We found that the 30 and 70 nm micelles demonstrated a comparable distribution in the tumour tissues, and both achieved ~20% of $V_{max}$ at 40 μm from the blood vessels at 1 h after co-injection (Fig. 5e). At 24 h after injection, both micelles had deeply penetrated the tumour (Fig. 5f), reaching over 40% of $V_{max}$ at 100 μm from the blood vessels (Fig. 5f). The 30 and 70 nm micelles also appeared to show comparable subcellular localization (Fig. 5f). These results suggest that the improvement in extravasation and penetration of 70 nm DACHPt/m by TGF-β-I caused the increased antitumour
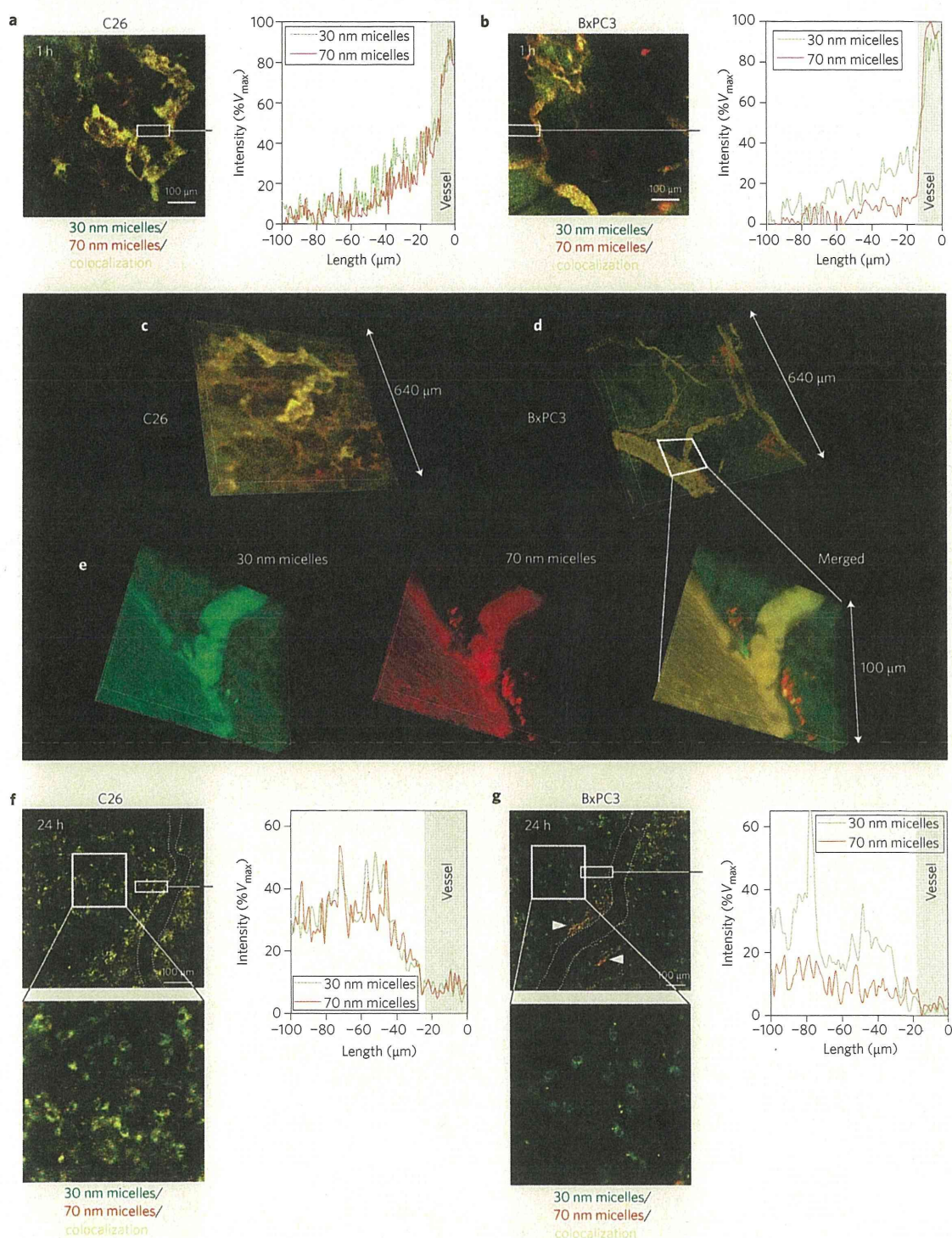
**Figure 4 | *In vivo* real-time microdistribution of DACHPt/m with different diameters in tumours. a,b**, Microdistribution of fluorescently labelled 30 nm (green) and 70 nm (red) micelles 1 h after injection into C26 (**a**) and BxPC3 (**b**) tumours. Their colocalization is shown in yellow. Right panels in **a** and **b** show fluorescence intensity profile from the blood vessel (0–10 μm; grey area) to the tumour tissue (10–100 μm) in the selected region (indicated by a white rectangle) expressed as a percentage of the maximum fluorescence intensity attained in the vascular region (%$V_{max}$). **c,d**, Z-stack volume reconstruction of C26 (**c**) and BxPC3 (**d**) tumours 1 h after co-injection of the fluorescent micelles. **e**, Magnification of the perivascular region (indicated by a white trapezium) of the z-stack volume image of BxPC3 tumours. **f,g**, Distribution of 30 and 70 nm micelles 24 h after injection into C26 tumours (**f**) and BxPC3 tumours (**g**). White arrows in **g** indicate 70 nm micelles localizing at perivascular regions. Right panels show fluorescence intensity profile from the blood vessel (0–10 μm; grey area) to the tumour tissue (10–100 μm) in the selected region (indicated by white rectangle).
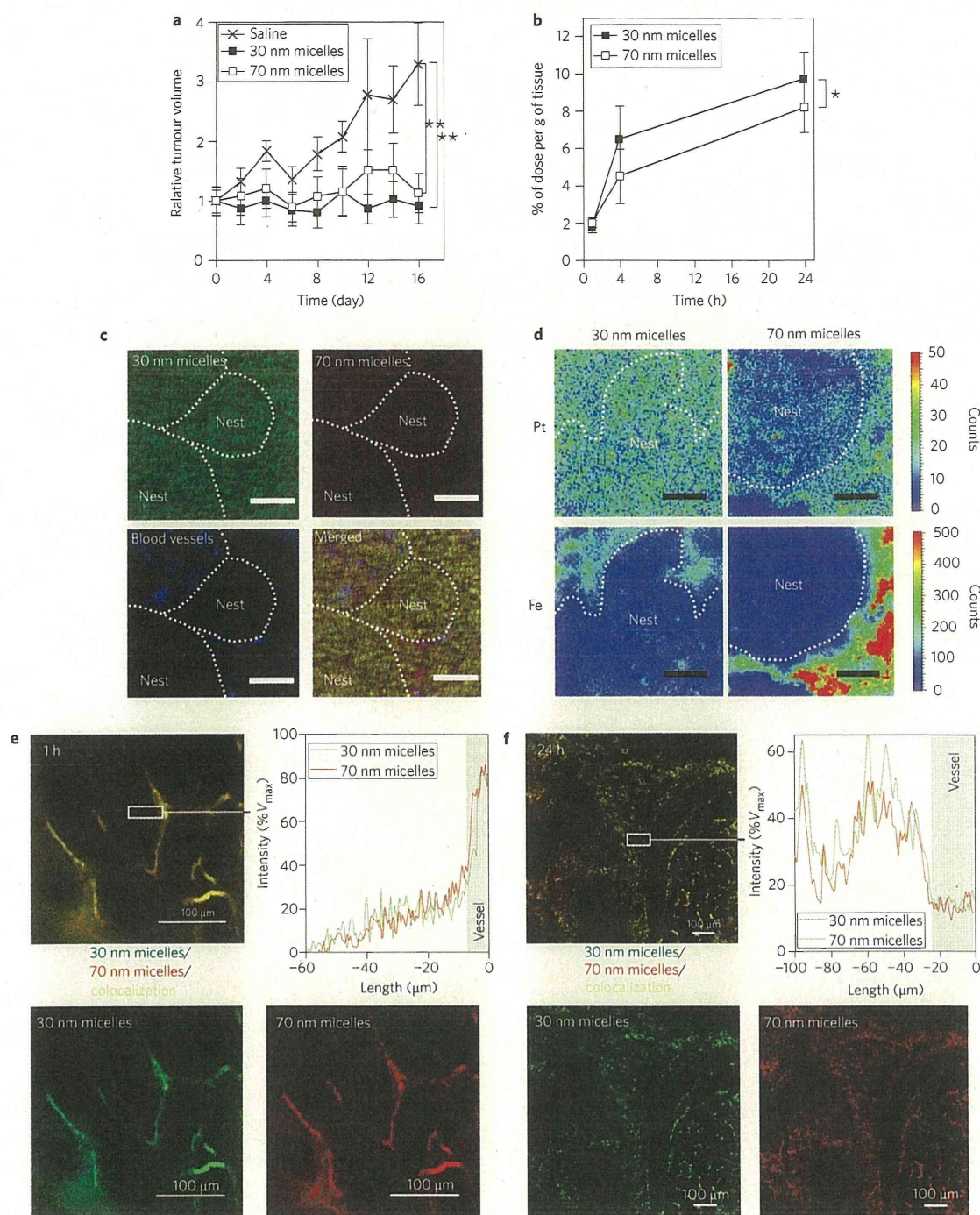
**Figure 5 | Effect of TGF-β inhibitor (TGF-β-I) on antitumour activity and tumour accumulation of DACHPt/m in BxPC3 tumours. a**, Graph showing relative tumour volume. Micelles (3 mg kg$^{-1}$) were injected on days 0, 4 and 8 and TGF-β-I on days 0, 2, 4, 6 and 8. **b**, Graph showing accumulation of 30 and 70 nm DACHPt/m in BxPC3 tumours after injection of TGF-β-I. Data are expressed as means ± s.e.m., $n = 6$. *$P > 0.05$; **$P < 0.01$. **c**, Fluorescent microscopy of tumour sections 24 h after co-administration of the fluorescent micelles and TGF-β-I. Scale bars, 50 μm. **d**, Platinum and iron mapping of tumour sections by μ-SR-XRF 24 h after administration of 30 and 70 nm micelles. Scale bars, 50 μm. **e,f**, Intravital distribution of 30 nm (green) and 70 nm (red) micelles in BxPC3 tumours 1 h (**e**) and 24 h (**f**) after co-injection of micelles and TGF-β-I. Their colocalization is shown in yellow. Right panels show fluorescence intensity profile from the blood vessel (grey area) to the tumour tissue in the selected region (indicated by a white rectangle).

activity, supporting the hypothesis that TGF-β inhibitors have great potential for enhancing the therapeutic efficacy of nanomedicines in hypopermeable tumours.

## Conclusions

The enhanced targeting of drugs to cancer cells within tumours by nanomedicines largely depends on size. We have shown that the

tumoricidal efficiency of long-circulating polymeric micelles depends on the size of the micelles and the permeability of the tumour. In hypervascular tumours with a highly permeable structure, sub-100 nm micellar nanomedicines showed no size-dependent restrictions on extravasation and penetration in tumours. In contrast, only nanomedicines smaller than 50 nm can penetrate poorly permeable hypovascular tumours. Furthermore, increasing the permeability of hypovascular tumours using TGF-β signalling inhibitor improved the accumulation and distribution of the larger 70 nm micelles, offering a way to enhance the efficacy of larger nanomedicines. Because efficient extravasation and tumour penetration are important prerequisites for targeting cancer cells, our findings are important for designing sophisticated nanomedicines that are capable of cell recognition and selective intracellular release of payloads.

## Materials and methods

**Materials, cell lines and animals.** Information regarding materials, cell lines (murine colon adenocarcinoma 26 (C26) cells and human pancreatic cancer BxPC3 cells) and animals is described in the Supplementary Information. All animal experiments were performed in accordance with the Guidelines for the Care and Use of Laboratory Animals as stated by the University of Tokyo.

**Tumour models.** BALB/c nude mice were inoculated subcutaneously with C26 cells ($1 \times 10^6$ cell ml$^{-1}$) to prepare the hyperpermeable tumour model, or with BxPC3 cells ($1 \times 10^7$ cell ml$^{-1}$) to prepare the hypopermeable tumour model. *In vivo* and *ex vivo* confocal microscopy, elemental mapping and antitumour activity studies were performed when the tumours were 50 mm in volume$^3$. Biodistribution studies were performed when the tumours were ~100 mm in volume$^3$.

**Preparation of PEG-*b*-P(Glu) block copolymer and P(Glu) homopolymer.** PEG-*b*-P(Glu) block copolymers and P(Glu) homopolymers were synthesized according to a previously described synthetic method[8] with a minor modification. Detailed procedures for polymer synthesis and characterization are described in the Supplementary Information. PEG-*b*-P(Glu) was fluorescently labelled by conjugating the Alexa 488 and Alexa 594 succinimidyl esters to the ω-amino group of the polymer in dimethyl sulfoxide. Detailed procedures are described in the Supplementary Information.

**Preparation and characterization of DACHPt/m with different diameters.** DACHPt/m with different diameters were prepared according to a previously described method with a slight modification[10,26,27]. Detailed procedures are described in the Supplementary Information. The size distribution of DACHPt/m was evaluated by DLS measurements at 25 °C, and the zeta potential of the micelles was measured in phosphate buffer at pH 7.4 using a Zetasizer Nano ZS90 (Malvern Instruments). The platinum content in the micelles was determined by ion-coupled plasma-mass spectrometry (ICP-MS) using a Hewlett Packard 4500 ICP-MS. Fluorescently labelled DACHPt/m was prepared in a similar manner with Alexa 488 or Alexa 594 labelled PEG-*b*-P(Glu). The stability of DACHPt/m with different diameters in Dulbecco's modified Eagle's medium (DMEM) containing 10% FBS at 37 °C was determined by DLS. The release rate of the micelles under similar conditions was studied by the dialysis method using a dialysis bag (molecular weight cutoff = 2,000). More detailed information is described in the Supplementary Information.

**Transmission electron microscopy.** The experimental procedure is described in the Supplementary Information.

**In vitro cytotoxicity assay.** The experimental procedure is described in the Supplementary Information.

**Antitumour activity assay.** Mice were treated three times intravenously at two-day intervals with 3 mg kg$^{-1}$ (on a platinum basis) of 30, 50, 70 and 100 nm DACHPt/m. Anti-tumour activity was evaluated in terms of tumour size ($V$), which was estimated by the equation

$$V = a \times b^2/2$$

where *a* and *b* are the major and minor axes of the tumour, respectively, as measured by a caliper. The statistical significance of different findings between the experimental and control groups was determined by analysis of variance (ANOVA) with Tukey's multiple comparison test. The results were considered statistically significant if two-tailed *P*-values were less than 0.05.

**Plasma clearance and organ and tumour accumulation of DACHPt/m with different diameters.** The experimental procedure is described in the Supplementary Information.

**Microdistribution and immunohistochemistry of fluorescently labelled DACHPt/m.** Mice bearing C26 or BxPC3 tumours were intravenously injected with Alexa 594-labelled 30, 50, 70 and 100 nm DACHPt/m at 100 µg per mouse on a platinum basis. Twenty-four hours later, tumours were collected and immediately frozen in an acetone/dry ice mixture. The frozen samples were further sectioned (thickness, 16 µm) in a cryostat, briefly fixed with cold acetone and then incubated with PECAM-1 antibody. Alexa 488 was used as the secondary antibody. Samples were observed using a Zeiss LSM510 Meta confocal microscope (Oberkochen). For H&E staining, the excised samples were fixed overnight in 4% paraformaldehyde and then paraffin-embedded to prepare them for the perfusion study in the tumour tissues. Samples were observed under an AX80 microscope (Olympus).

**Element array analysis using µ-X-ray fluorescence.** SR-XRF was used to determine DACHPt as well as iron distribution in sections of solid tumours (C26 or BxPC3) at 24 h post-intravenous injection of 30 and 70 nm DACHPt/m[36]. The detailed experimental procedure is described in the Supplementary Information.

**In vivo confocal laser scanning microscopy (in vivo CLSM).** Mice bearing C26 or BxPC3 tumours were intravenously co-injected with fluorescently labelled 30 and 70 nm DACHPt/m at a dose of 10 mg kg$^{-1}$. The 30 nm micelles were labelled with Alexa 488, and the 70 nm micelles were labelled with Alexa 594. The *in vivo* CLSM observation of tumour tissues was performed according to a previously reported method[28,34]. All *in vivo* picture acquisitions were performed using a Nikon A1R confocal laser scanning microscope system attached to an upright ECLIPSE FN1 (Nikon). The 30-nm-diameter micelles were detected using 488/510 nm excitation/emission filters, and the signal from the 70 nm micelles was acquired with 560/620 nm excitation/emission filters.

**Enhancement of tumour permeability by treatment with a TGF-β inhibitor.** The effect of TGF-β inhibitor on the accumulation and antitumour activity of DACHPt/m was determined using the methods already described. For the antitumour activity experiment, BxPC3-bearing mice were administered intraperitoneal injections of TGF-β inhibitor LY364947 at 1 mg kg$^{-1}$ every second day. For tumour accumulation studies, BxPC3-bearing mice received an intraperitoneal injection of the TGF-β inhibitor at 1 mg kg$^{-1}$ at 1 h before co-injection of the 30 and 70 nm micelles.

## References

1. Duncan, R. The dawning era of polymer therapeutics. *Nature Rev. Drug Discov.* **2**, 347–360 (2003).
2. Ferrari, M. Cancer nanotechnology: opportunities and challenges. *Nature Rev. Cancer.* **5**, 161–171 (2005).
3. Torchilin, V. P. Recent advances with liposomes as pharmaceutical carriers. *Nature Rev. Drug Discov.* **4**, 145–160 (2005).
4. Davis, M. E., Chen, Z. & Shin, D. Nanoparticle therapeutics: an emerging treatment modality for cancer. *Nature Rev. Drug Discov.* **7**, 771–782 (2008).
5. Kataoka, K., Harada, A. & Nagasaki, Y. Block copolymer micelles for drug delivery: design, characterization and biological significance. *Adv. Drug Deliv. Rev.* **47**, 113–131 (2001).
6. Nishiyama, N. & Kataoka, K. Current state, achievements, and future prospects of polymeric micelles as nanocarriers for drug and gene delivery. *Pharmacol Ther.* **112**, 630–648 (2006).
7. Matsumura, Y. & Maeda, H. A new concept for macromolecular therapeutics in cancer chemotherapy: mechanism of tumouritropic accumulation of proteins and the antitumour agent SMANCS. *Cancer Res.* **46**, 6387–6392 (1986).
8. Nishiyama, N. *et al.* Novel cisplatin-incorporated polymeric micelles can eradicate solid tumours in mice. *Cancer Res.* **63**, 8977–8983 (2003).
9. Bae, Y. *et al.* Preparation and biological characterization of polymeric micelle drug carriers with intracellular pH-triggered drug release property: tumor permeability, controlled subcellular drug distribution, and enhanced *in vivo* antitumor efficacy. *Bioconjug. Chem.* **16**, 122–130 (2005).
10. Cabral, H., Nishiyama, N. & Kataoka, K. Optimization of (1,2-diamino-cyclohexane) platinum(II)-loaded polymeric micelles directed to improved tumour targeting and enhanced antitumour activity. *J. Control. Release* **121**, 146–155 (2007).
11. Maruyama, K., Ishida, O., Takizawa, T. & Moribe, K. Possibility of active targeting to tumor tissue with liposome. *Adv. Drug Deliv. Rev.* **40**, 89–102 (1999).
12. Lammers, T. *et al.* Image-guided and passively tumor-targeted polymeric nanomedicines for radiochemotherapy. *Br. J. Cancer* **99**, 900–910 (2008).
13. Matsumura, Y. & Kataoka, K. Preclinical and clinical studies of anticancer agent-incorporating polymer micelles. *Cancer Sci.* **100**, 572–579 (2009).
14. Matsumura, Y. Preclinical and clinical studies of NK012, an SN-38-incorporating polymeric micelles, which is designed based on EPR effect. *Adv. Drug Deliv. Rev.* **63**, 184–192 (2011).

15. Working, P. K. *et al.* Pharmacokinetics, biodistribution and therapeutic efficacy of doxorubicin encapsulated in stealth liposomes (DOXIL). *J. Liposome Res.* **4**, 667–687 (1994).
16. Northfelt, D. W. *et al.* Pegylated-liposomal doxorubicin versus doxorubicin, bleomycin, and vincristine in the treatment of AIDS-related Kaposi's sarcoma: results of a randomized phase III clinical trial. *J. Clin. Oncol.* **16**, 2445–2451 (1998).
17. Gradishar, W. J. *et al.* Phase III trial of nanoparticle albumin-bound paclitaxel compared with polyethylated castor oil-based paclitaxel in women with breast cancer. *J. Clin. Oncol.* **23**, 7794–7803 (2005).
18. Uster, P. S., Working, P. K. & Vaage, J. Pegylated liposomal doxorubicin (DOXIL(R), CAELYX(R)) distribution in tumour models observed with confocal laser scanning microscopy. *Int. J. Pharm.* **162**, 77–86 (1998).
19. Unezaki, S. *et al.* Direct measurement of the extravasation of polyethyleneglycol-coated liposomes into solid tumor tissue by *in vivo* fluorescence microscopy. *Int. J. Pharm.* **144**, 11–17 (1996).
20. Kano, M. R. *et al.* Improvement of cancer-targeting therapy, using nanocarriers for intractable solid tumours by inhibition of TGF-β signaling. *Proc. Natl Acad. Sci. USA* **104**, 3460–3465 (2007).
21. Dreher, M. *et al.* Tumour vascular permeability, accumulation, and penetration of macromolecular drug carriers. *J. Natl Cancer Inst.* **98**, 330–343 (2006).
22. Perrault, S. D., Walkey, C., Jennings, T., Fischer, H. C. & Chan, W. C. W. Mediating tumour targeting efficiency of nanoparticles through design. *Nano Lett.* **9**, 1909–1915 (2009).
23. Aliabadi, H. M. & Lavasanifar, A. Polymeric micelles for drug delivery. *Exp. Opin. Drug. Deliv.* **3**, 139–162 (2006).
24. Matsumura, Y. *et al.* Phase I clinical trial and pharmacokinetic evaluation of NK911, a micelle-encapsulated doxorubicin. *Br. J. Cancer* **91**, 1775–1781 (2004).
25. Plummer, R. *et al.* A phase I clinical study of cisplatin-incorporated polymeric micelles (NC-6004) in patients with solid tumours. *Br. J. Cancer* **104**, 593–598 (2011).
26. Cabral, H., Nishiyama, N., Okazaki, S., Kato, Y. & Kataoka, K. Preparation and biological properties of dichloro(1,2-diaminocyclohexane)platinum(II) (DACHPt)-loaded polymeric micelles. *J. Control. Release* **101**, 223–232 (2005).
27. Nishiyama, N. & Kataoka, K. Preparation and characterization of size-controlled polymeric micelle containing *cis*-dichlorodiammineplatinum(II) in the core. *J. Control. Release* **74**, 83–94 (2001).
28. Murakami, M. *et al.* Improving drug potency and efficacy by nanocarrier-mediated subcellular targeting. *Sci. Transl. Med.* **3**, 64ra2 (2011).
29. Alexis, F., Pridgen, E., Molnar, L. K. & Farokhzad, O. C. Factors affecting the clearance and biodistribution of polymeric nanoparticles. *Mol. Pharm.* **5**, 505–515 (2008).
30. Verma, A. *et al.* Surface-structure-regulated cell-membrane penetration by monolayer-protected nanoparticles. *Nature Mater.* **7**, 588–595 (2008).
31. Kano, M. R. *et al.* Comparison of the effects of the kinase inhibitors imatinib, sorafenib, and transforming growth factor-β receptor inhibitor on extravasation of nanoparticles from neovasculature. *Cancer Sci.* **100**, 173–180 (2009).
32. Takahashi, Y. *et al.* Significance of vessel count, vascular endothelial growth factor, and its receptor (KDR) in intestinal-type gastric cancer. *Clin. Cancer Res.* **2**, 1679–1684 (1996).
33. Sofuni, A. *et al.* Differential diagnosis of pancreatic tumours using ultrasound contrast imaging. *J. Gastroenterol.* **40**, 518–525 (2005).
34. Matsumoto, Y. *et al.* Direct and instantaneous observation of intravenously injected substances using intravital confocal micro-videography. *Biomed. Optics Exp.* **1**, 1209–1216 (2010).
35. Choi, H. S. *et al.* Renal clearance of quantum dots. *Nature Biotechnol.* **25**, 1165–1170 (2007).
36. Terada, Y. *et al.* Construction and commissioning of BL37XU at SPring-8. *AIP Conf. Proc.* **705**, 376–379 (2004).

## Acknowledgements

## Author contributions

H.C. designed and performed all the experiments. Y.M. assisted with *in vivo* confocal microscopies. K.M. and Y.T. helped in the μ-X-ray fluorescence measurements. Q.C. performed transmission electron microscopy of the micelles. M.M and M.K. aided in the biodistribution experiments. H.C. wrote the manuscript. M.R.K., K.M. and M.U. commented on the manuscript. N.N. and K.K. edited the manuscript. K.K., with help from N.N., supervised the whole project.

## Additional information

NANOMEDICINE
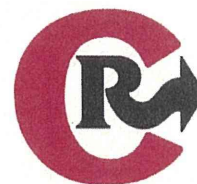
# Disulfide crosslinked polyion complex micelles encapsulating dendrimer phthalocyanine directed to improved efficiency of photodynamic therapy

Stephanie Herlambang [a], Michiaki Kumagai [b,c], Takahiro Nomoto [d], Souta Horie [b], Shigeto Fukushima [b], Makoto Oba [e], Kozo Miyazaki [b], Yuji Morimoto [f], Nobuhiro Nishiyama [b,g,*], Kazunori Kataoka [a,b,g,**]

[a] Department of Materials Engineering, Graduate School of Engineering, The University of Tokyo, 7-3-1 Hongo, Bunkyo-ku, Tokyo 113-8656, Japan
[b] Division of Clinical Biotechnology, Center for Disease Biology and Integrative Medicine, Graduate School of Medicine, The University of Tokyo, 7-3-1 Hongo, Bunkyo-ku, Tokyo 113-0033, Japan
[c] Innovation Center for Medical Redox Navigation, Kyushu University, 3-1-1 Maidashi, Higashi-ku, Fukuoka, Fukuoka 812-8582, Japan
[d] Department of BioEngineering, Graduate School of Engineering, The University of Tokyo, 7-3-1 Hongo, Bunkyo-ku, Tokyo 113-8656, Japan
[e] Department of Clinical Vascular Regeneration, Graduate School of Medicine, The University of Tokyo, 7-3-1 Hongo, Bunkyo-ku, Tokyo 113-8655, Japan
[f] Department of Integrative Physiology and Bio-Nano Medicine, National Defense Medical College, Namiki 3-2, Tokorozawa, Saitama 359-8513, Japan
[g] Center for NanoBio Integration, The University of Tokyo, 7-3-1 Hongo, Bunkyo-ku, Tokyo 113-8656, Japan

## ARTICLE INFO

## ABSTRACT

Dendrimer phthalocyanine (DPc)-loaded polyion complex micelle (DPc/m) has been developed as photosensitizer (PS) formulation in photodynamic therapy (PDT). Incorporation of DPc into the micelle showed significant enhancement in the *in vitro* photocytotoxicity. Also, introduction of disulfide crosslinking in the micellar core further improved the *in vitro* PDT effect of DPc/m. Here, we aim to analyze the mechanism of the enhanced photocytotoxicity of DPc/m, particularly focusing on the photochemical reactions during photoirradiation. As a result, DPc/m has been shown to protect DPc from photobleaching induced by the reactions with serum proteins, although DPc were considerably quenched in the micellar core. Furthermore, the introduction of disulfide crosslinking into the micellar core has demonstrated to improve the efficiency of reactive oxygen species (ROS) production by DPc in the micellar core as well as more effectively prevent the photobleaching of DPc. These effects might lead to effective photochemical reactions by DPc/m, which may account for the enhanced photocytotoxicity. Our findings provide useful knowledge in designing PS formulations for effective PDT.

© 2011 Elsevier B.V. All rights reserved.

## 1. Introduction

Photodynamic therapy (PDT) is a potent targeted cancer treatment against superficial cancers including lung, oesophageal, gastric and cervical cancers [1–3]. Major advantages of PDT over current therapies and treatments are less invasiveness compared with surgery and precise targeting through selective light irradiation to the diseased sites [4,5]. The treatment can be repeated several times at the same site if necessary [3]. PDT is based on the accumulation of photosensitizers (PSs) in malignant tissues. Upon photoirradiation at the specific wavelength, PSs convert oxygen into cytotoxic reactive oxygen species (ROS), which oxidize (photodamage) subcellular organelles and biomolecules, leading to light-induced cell death [1–5].

Regarding the photochemical reactions in PDT, PSs in the singlet ground state ($S_0$) absorb a photon and are excited to the short-lived singlet state ($S_1$). The PSs in the singlet excited state are converted to the metastable triplet excited state ($T_1$) through the intersystem crossing. This triplet excited state of PSs induces the photochemical reactions via type I or type II mechanisms. The type I reaction involves the transfer of protons or electrons from PSs to other molecules to produce free radicals or electron transfer. The reaction with oxygen molecules generates superoxide ($O_2^-$) and peroxide ($O_2^{2-}$) anions. The type II reaction involves the energy transfer from PSs to molecular oxygen in the triplet ground state ($^3O_2$), leading to the formation of highly reactive singlet oxygen ($^1O_2$). The type II reaction has been reported to be a more important process in PDT [3].

Recently, nanocarriers such as liposomes and polymeric micelles have received considerable attention as a PS formulation [6–14], because they have potentials to effectively and selectively accumulate in the tumor tissue due to the Enhanced Permeability and Retention (EPR) effect [15]. In this regard, we have developed polymeric micelles encapsulating dendrimer phthalocyanine (DPc, Fig. 1A). DPc possesses several advantages compared with conventional PSs. In general, conventional PSs easily form aggregate through their π–π
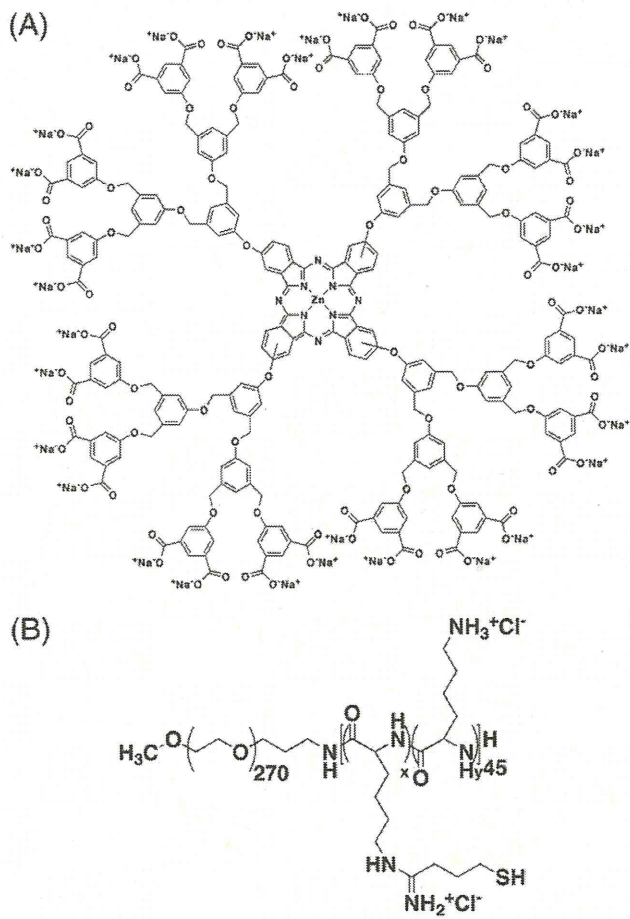
**Fig. 1.** Chemical structures of anionic dendrimer phthalocyanine (DPc) (A) and thiolated poly(ethylene glycol)-*block*-poly(L-lysine) [PEG–PLys(IM)] copolymer (B).

stacking and hydrophobic interactions, resulting reduced ROS production due to the self-quenching of the excited state. By contrast, DPc possesses the large dendritic wedge protecting the center phthalocyanine molecules from the self-quenching, allowing the effective photochemical reactions even at a high concentration. Also, 32 carboxyl groups on the periphery of DPc enabled the formation of the polyion complex (PIC) micelle with oppositely charged poly(ethylene glycol)-poly(L-lysine) (PEG-PLys) block copolymers in aqueous media [8,9]. We have demonstrated that the DPc-loaded micelle (DPc/m) showed remarkably enhanced photocytotoxicity than DPc alone and potent *in vivo* antitumor activity without skin photocytotoxicity in tumor-bearing mice [9]. However, the mechanisms of the enhanced photocytotoxicity of DPc/m remain to be clarified yet.

In the present paper, we aimed to analyze the mechanisms of the PDT effect of DPc/m from the standpoint of photochemical properties, cellular uptake and intracellular ROS production. We found that DPc/m might protect DPc from photobleaching in the biological media, leading to improved photochemical reactions. On the other hand, we report here a novel design of DPc/m for further enhancement of the PDT effect, that is, introduction of disulfide crosslinking into the micellar core. Recently, increasing attention has been paid on disulfide-crosslinked nanocarriers, because the disulfide crosslinking can improve the stability of the nanostructure in biological media while maintaining the activity of the incorporated bioactive com-

pounds [16,17]. In the present study, we demonstrate that disulfide crosslinked DPc/m show further enhanced *in vitro* PDT effect, which may be attributed to improved efficiency of ROS production and further reduction of the photobleaching in the micellar core.

## 2. Materials and methods

### 2.1. Materials

*N,N*-Diisopropylethylamine (DIEA), dithiothreitol (DTT), and LiCl were purchased from WAKO Pure Chemical Industries (Osaka, Japan). 2-Iminothiolane was purchased from PIERCE Co., Inc. (Rockford, IL). *N*-Methyl-2-pyrrolidone (NMP), dimethyl sulfoxide (DMSO), and *N,N*-dimethylformamide (DMF) were purchased from Nacalai Tesque Inc. (Kyoto, Japan). $N^\epsilon$-Trifluoroacetyl-L-lysine [Lys(TFA)] and bis(trichloromethyl)carbonate (triphosgene) were purchased from Sigma-Aldrich Co., Inc. (St. Louis, MO, USA) and Tokyo Chemical Industry Co., Ltd. (Tokyo, Japan), respectively. Lys(TFA) *N*-carboxyanhydride [Lys(TFA)-NCA] was synthesized by the Fuchs-Farthing method using triphosgene [18]. α-Methoxy-ω-amino-poly(ethylene glycol) ($CH_3O$-PEG-$NH_2$; $Mw = 12\,000$) was purchased from NOF Corporation (Tokyo, Japan). The synthesis of DPc has been reported previously [8]. The synthesized DPc is composed of the 2nd generation aryl ether dendrimer with a Zn(II)-phthalocyanine center and 32 carboxylic groups on its periphery.

## 2.2. Synthesis of poly(ethylene glycol)-poly(L-lysine) block copolymer (PEG-PLys)

Lys(TFA)-NCA (10.72 g, 40 mmol, 50 equiv to CH$_3$O-PEG-NH$_2$) in DMSO was added to CH$_3$O-PEG-NH$_2$ (9.60 g, 800 μmol) in DMSO and incubated at 35 °C for 2 days. The reactant polymer was precipitated into diethylether and vacuum-dried to obtain PEG-PLys(TFA). Molecular weight distribution of PEG-PLys(TFA) was narrow as Mw/Mn = 1.11, which was determined by gel permeation chromatography [columns: TSK-gel G3000HHR, G4000HHR (Tosoh, Yamaguchi, Japan); eluent: DMF containing 10 mM LiCl; flow rate: 0.8 ml/min; detector: refractive index (RI); temperature: 40 °C]. NaOH solution (1 N, 10 mL) was added to 1 g of PEG-PLys(TFA) in methanol (100 mL) and incubated at 35 °C for 12 h. The reacted polymer was purified by dialysis sequentially against 0.01 N HCl and distilled water, and then lyophilized to obtain PEG-PLys. The composition of the block copolymer was determined by $^1$H NMR from the peak intensity ratios of methylene protons of PEG (OCH$_2$CH$_2$: δ = 3.7 ppm) and β-, γ-, and δ-methylene protons of PLys ((CH$_2$)$_3$: δ = 1.3 to 1.9 ppm). The polymerization degree of PLys in block copolymer was calculated to be 45.

## 2.3. Synthesis of PEG-PLys(IM)

PEG-PLys(IM) (Fig. 1B) was synthesized by reaction of primary amino group in side chains of PLys segments with 2-iminothiolane as previously reported [19,20]. Briefly, PEG-PLys and 2-iminothiolane were separately dissolved in NMP containing 5 wt.% LiCl. Then, the solutions were mixed at various molar ratios of 2-iminothiolane/Lys up to 2.0 and incubated at 25 °C for 18 h after addition of DIEA (5 equivalent relative to lysine units). The mixtures were purified by precipitation into a 15-fold excess of diethylether. Precipitated polymer was redissolved in 0.01 N HCl, dialyzed against distilled water (MWCO: 12,000–14,000), and lyophilized to obtain PEG-PLys (IM) copolymer. The degree of substitution for each PEG-PLys(IM) was determined by $^1$H NMR (D$_2$O, 25 °C) from peak intensity ratios of β-, γ-, and δ-methylene protons of PLys (δ = 1.3 to 1.9 ppm) to the protons of trimethylene units of mercaptopropyl groups (δ = 2.1 to 2.8 ppm). The calculated substitution degrees are shown as PEG-PLys (IM$_{x\%}$), where x stands for the substitution degree. In this study, PEG-PLys(IM)'s with thiol substitution degrees of 13%, 28% and 39% were synthesized and used to prepare the crosslinked DPc-loaded micelles, which were abbreviated as DPc/m/c-13, -28, and -39, respectively.

## 2.4. Preparation of non-crosslinked and crosslinked polyion complex micelles

A non-crosslinked polyion complex micelle (DPc/m) was obtained by simply mixing PEG-PLys (6.65 mg/ml) and DPc (3 mg/ml) solutions in 10 mM phosphate buffered solution (pH 7.4) at 37 °C for 30 min (final DPc concentration: 267 μM). To prepare the crosslinked polyion complex micelles (DPc/m/c's), PEG-PLys(IM) solutions were incubated in a DTT solution (100 mM in 10 mM phosphate buffered solution, pH 7.4) at 37 °C for 30 min to reduce the disulfide bonds. Then, polymer solution was added to DPc solution to form polyion complex micelles. The mixing ratio of positive charge to negative charge was fixed at 0.9. After 1 h incubation at 37 °C, thiol groups were oxidized to form disulfide crosslinks by dialysis against 10 mM phosphate buffered solution (PBS) (pH 7.4) containing 0.5% DMSO at 25 °C for 2 days, followed by 2 days of additional dialysis against 10 mM PBS (pH 7.4) for the removal of DMSO. For dialysis, the membrane of molecular weight cut-off size of 8000 Da (Mini Dialysis Kit, GE Heathcare, Piscataway, NJ) was used. We confirmed that there was no loss of materials (DPc and block copolymers) during the dialysis procedure (data not shown) (final DPc concentration: 267 μM). Furthermore, remaining free thiol groups after the formation

of crosslinked micelles were determined to be 23.5 to 33.3% using Ellman's method [21], suggesting >70% of thiol groups of PEG-PLys (IM) are assumed to form disulfide linkages in the micellar core.

## 2.5. ζ-potential, dynamic light scattering (DLS), and UV–vis absorption measurements

The ζ-potential of the polyion complex micelles at 37 °C was measured by a Zetasizer NanoZS instrument equipped with a DTS5001 cell (Malvern Instruments Ltd., Worcestershire, UK) with 532 nm laser. The size distribution of the polyion complex micelles was examined by dynamic light scattering (DLS) DLS-7000 (Otsuka Electronics Co., Ltd., Osaka, Japan) equipped with GLG3050 488 nm Ar laser (NEC Co., Ltd., Tokyo, Japan). The UV–vis absorption spectra were measured using a V-550 spectrophotometer (JASCO, Tokyo, Japan).

## 2.6. Cell culture and cytotoxicity assay

Human lung adenocarcinoma A549 cells were obtained from Riken Bioresource Center Cell Bank (Tsukuba, Japan). A549 cells were maintained in Dulbecco's modified Eagle medium (DMEM, Invitrogen Corporation, Carlsbad, CA, USA) containing 10% fetal bovine serum (FBS) in a humidified atmosphere containing 5% CO$_2$ at 37 °C. The light-induced cytotoxicity (photocytotoxicity) of each photosensitizing agent was evaluated as follows: In a darkened room, the cells were incubated with photosensitizing agents for 24 h. After washing with PBS and medium replacement, the cells were photoirradiated using a halogen lamp. The culture plate was irradiated with broad-band visible light using a halogen lamp equipped with a filter passing light of 400–700 nm (fluence rate: 3.0 mW/cm$^2$; irradiation time: 15, 30, 45, and 60 min; fluence: 2.7–10.8 J/cm$^2$). The cell viability was evaluated by MTT assay 48 h after photoirradiation.

## 2.7. Analysis of cellular uptake of DPc

$^{125}$I was labeled on the benzene groups in DPc through oxidation reaction using chloramine T [22]. One microliter of Na$^{125}$I (46 pmol, 0.1 mCi, PerkinElmer Life & Analytical Sciences, Boston, MA, USA) in 10 μM NaOH (pH 8–11) was mixed with 1 ml of 10 mM sodium phosphate buffered solution (pH 7.4) of DPc (2.7 μmol, 15 mg/ml). Ten microliter of chloramine T (180 nmol, 5.0 mg/mL) in 10 mM sodium phosphate buffered solution (pH 7.4) was then added to the DPc solution at 1 min after mixing with NaI. After incubation for 4 min at room temperature, the reaction was stopped by the addition of a 20-μl volume of cysteine (280 nmol, 1.7 mg/ml) in 10 mM sodium phosphate buffer solution (pH 7.4). The DPc samples were 4 times purified through the PD MidiTrap G-10 column (GE Healthcare Bio-Sciences AB, Uppsala, Sweden) using 10 mM sodium phosphate buffer solution (pH 7.4) as an eluent prior to a cellular uptake study. For cellular uptake experiments, A549 cells were seeded on 6-well culture plates (5 × 10$^5$ cells/well) and incubated overnight in DMEM containing 10% FBS. The polyion complex micelle incorporating the mixture of non-labeled and $^{125}$I-labeled DPc was applied to each well (10 μM DPc/well). After 24 h incubation, the medium was removed and the cells were washed 3 times with Dulbecco's PBS. The cells were incubated with 1 mL of trypsine-EDTA (Sigma-Aldrich Corporation, St. Louis, MO, USA) for 15 min at 37 °C, and collected. Note that the treatment with trypsine-EDTA might minimize the contribution from the non-internalized DPc fraction associated on the cell surface. Radioactivities in the collected samples were measured by a γ-counter (COBRA II Auto-GAMMA MODEL D50 05, Packard Instrument Company, Meriden, CT, USA) with a counting time of 1 min. The results are presented as a mean and standard deviation obtained from three samples.

## 2.8. Measurement of oxygen consumption efficiency

The oxygen consumption amount was measured using a Clark-type oxygen electrode with a tip diameter of 2 cm (OM-51-L1, HORIBA, Ltd., Kyoto, Japan). The electrode was inserted into 10 mM PBS (pH = 7.4), which contained 26.7 μM of DPc in free or micelle form and 10% FBS as an ROS acceptor, so that the tip was 1 cm above the bottom of the solution. Semiconductor laser light (685 nm; FWHM 10 nm, 50 mW) was used for light irradiation. The solution was stirred at a constant rate and not exposed to the atmosphere. Before each measurement, the system was calibrated in saline bubbled with oxygen gas, in which the partial oxygen pressure was assumed to be 150 mm Hg.

The logarithmic value of the relative change of $pO_2$ vs. time was a linear function when the $O_2$ loss was within 5% of the initial $O_2$ concentration. ROS production was calculated as initial rates of oxygen loss as follows [23]:

$$-d[O_2]_t / dt = k\ [O_2]_i$$

where $[O_2]_i$ is the initial $O_2$ concentration in solution, $[O_2]_t$ is the $O_2$ concentration in solution at time t, and k is the slope of $\ln([O_2]_t/[O_2]_i)$ vs. time. The gradient of the linear line (k) is proportional to the light intensity, as well as the light absorption coefficient and quantum yield of the sensitizer. Thus, k value is correlated with the efficiency of the ROS production.

## 2.9. Photobleaching effect

To evaluate the photobleaching effect, we measured the absorbance at Q-band peak of DPc (6.69 μM) upon laser irradiation in the media solution containing 10% FBS under the condition saturated with argon gas or oxygen gas.

## 2.10. Observation of intracellular ROS production

The ROS production in the mitochondria in A549 cells was evaluated by MitoSOX Red reagent (Invitrogen Corporation, Carlsbad, CA, USA), which rapidly accumulates in the mitochondria and exhibits fluorescence upon oxidation by superoxide and other ROS. After 24-h incubation with DPc, DPc/m or DPc/m/c, the cells were incubated with MitoSOX Red (5 μM) for 10 min at 37 °C. Then, the fluorescence of MitoSOX Red in living cells after photoirradiation using halogen lamp (fluence rate 3.0 mW/cm$^2$) was observed by confocal laser scanning microscopy (CLSM) (LSM510META, Carl Zeiss, Oberkochen, Germany).

## 3. Results

### 3.1. Formation of polyion complex micelles

The sizes and ζ-potentials of the non-crosslinked DPc-loaded micelle (DPc/m) and crosslinked DPc-loaded micelle (DPc/m/c) were evaluated by DLS and laser-doppler electrophoresis, respectively. Table 1 summarizes the cumulant diameter and ζ-potentials of DPc/m and DPc/m/c. The cumulant diameters of all the micelles were 30–40 nm with a narrow size distribution (polydispersity index (PDI) < 0.1), and decreases slightly as the IM substitution degree of PEG-PLys (IM) increases. Since introduction of 2-iminothiolane into PEG-PLys does not alter the number of positive charges in the polymer strand because of the formation of the cationic amidine group (Fig. 1B), the number ratios of DPc to block copolymers were kept constant in all the polyion complex micelles prepared at the charge ratio of 0.9, regardless of the thiolation degree. Note that as we previously reported non-crosslinked DPc/m contained 77 DPc molecules in the core [9]. The ζ-potentials of all the micelles were kept neutral, which

**Table 1**
Size, size distribution and ζ-potential of non-crosslinked and crosslinked DPc-loaded polyion complex micelle (DPc/m and DPc/m/c).

| Thiolation degree (%) | 0 | 13 | 28 | 39 |
|---|---|---|---|---|
| Cumulant diamter (nm) | 39 | 36 | 35 | 35 |
| Polydispersity index ($\mu/\Gamma^2$) | 0.096 | 0.042 | 0.058 | 0.093 |
| ζ-potential (mV) | −0.45 | −1.5 | −1.7 | −1.9 |

is consistent with the formation of the PEG palisade surrounding the micellar core. Furthermore, the stability of DPc/m and DPc/m/c in 10 mM phospate buffered solutions (pH 7.4) containing different NaCl concentrations (75–1000 mM) at 37 °C was studied by measuring the light scattering intensity of the micelle solution (Supporting Information). As a result, DPc/m and DPc/m/c maintained >80 and >90% of their initial light scattering intensity even at 1 M NaCl concentration, respectively (Figure S1). Thus, it appears that the non-crosslinked micelles were already sufficiently stable against ionic strength.

### 3.2. Visible light absorption spectrum

The absorption spectra of DPc, DPc/m, and DPc/m/c are shown in Fig. 2. DPc exhibits two Q-band absorbance peaks, one at 630 nm originates from the aggregated state, and the other at 685 nm originates from the monomeric state of phthalocyanine core units [24–26]. DPc alone showed a strong absorbance at 685 nm, suggesting the monomeric state of DPc in the aqueous solution. When DPc was incorporated into polyion complex micelles, the absorbance maximum of Q-band shifted to 630 nm, suggesting the interaction of the phthalocyanine core units between DPc in the micellar core. By introducing the disulfide crosslinking into the micellar core, the absorbance at 685 nm increased. These results suggest that disulfide crosslinking might weaken the interaction between DPc in the micelle.

### 3.3. Photocytotoxicity

The photocytotoxicity of DPc, DPc/m, and DPc/m/c was assessed against A549 cells (supporting information Figure S2). Table 2 summarizes the 50% cell growth inhibitory concentrations (IC$_{50}$) of DPc, DPc/m, and DPc/m/c under different photoirradiation conditions. Note that none of the photosensitizing agents showed dark cytotoxicity (Figure S2). The DPc/m showed remarkably improved photocytotoxicity compared with free DPc (Table 2 and Figure S2). After 60 min irradiation, the photocytotoxicity of DPc/m was 10 times higher compared to that of DPc. Further improvement in photocytotoxicity was observed by the introduction of disulfide crosslinking into the micellar core. The DPc/m/c-13 and DPc/m/c-28 achieved a more than 10-fold greater photocytotoxicity than DPc/m at
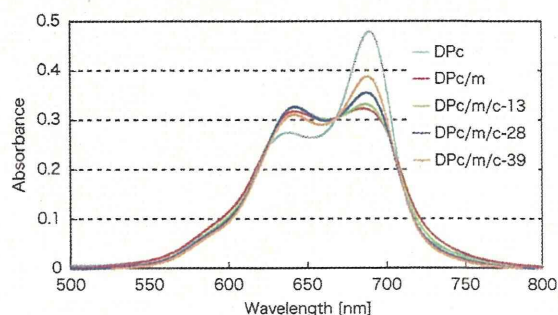
**Fig. 2.** UV–vis absorption spectra of DPc, DPc/m and DPc/m/c in 10 mM phosphate buffered solution (pH 7.4).

10.8 J/cm². However, the enhancement decreased with the introduction of 39% IM units to only 2-fold higher photocytotoxicity compared to DPc/m. Moreover, the photosensitizing agents exhibited different irradiation time-dependent increase in the photocytotoxicity (Table 2). When the irradiation time increased from 15 min to 60 min, DPc/m/c-13 and -28 showed 20- and 14-fold increases in photocytotoxicity while DPc/m/c-39 showed only 2.5-fold increase in photocytotoxicity.

### 3.4. Cellular uptake

As shown in Fig. 3, the cellular uptake of DPc increased up to 9 times by its incorporation into the micelles (DPc/m). Further improvement of cellular uptake was observed by the introduction of the disulfide crosslinking (Fig. 3). The DPc/m/c-13, 28, and 39 showed 1.3, 2.3 and 1.9 times higher cellular uptake of DPc compared with DPc/m. It is assumed that the disulfide crosslinking might increase the stability of the micellar structure in the cell culture media, resulting in an increased cellular uptake of DPc.

### 3.5. Measurement of oxygen consumption

The oxygen consumption of the DPc, DPc/m, and DPc/m/c upon photoirradiation at 685 nm was observed to evaluate the efficiency of the photochemical reactions. Under light irradiation, PSs produce ROS such as singlet oxygen and superoxide anion. The partial oxygen pressure ($pO_2$) changes in the medium containing DPc, DPc/m, or DPc/m/c and 10% FBS were recorded during photoirradiation (Fig. 4A). In this experiment, FBS plays a role of antioxidant scavengers as previously reported [27]. Fig. 4B shows the logarithmic plots of relative change in $pO_2$ vs. irradiation time, when irradiation time was within 200 s. The initial gradients of $\ln([O_2]_t/[O_2]_{initial})$ (k value) (dotted linear lines in Fig. 4B) are correlated with the efficiency of the ROS production. The k values and the oxygen consumption amount after 1000 s of laser irradiation were summarized in Table 3.

As shown in Table 3, DPc/m showed 3.4-fold lower k value compared with DPc. However, introduction of the disulfide cross-linking resulted in improvement of the k values, i.e., DPc/m/c-13, -28, and -39 showed 1.4, 1.9, and 2.0-fold higher k values compared with DPc/m, respectively. The k values of DPc, DPc/m, and DPc/m/c seem to be related with their absorbance at 685 nm ($A_{685}$) obtained in Fig. 2 (Table 3). Furthermore, the $k/A_{685}$ values, which are correlated with the quantum yield of ROS production, were calculated in Table 3. Incorporation of DPc into the PIC micelle resulted in 2.4-fold decrease in the $k/A_{685}$ value; however, introduction of the disulfide cross-linking led to recovery of the $k/A_{685}$ values, i.e., DPc/m/c-13, -28 and -39 showed 1.4, 1.8 and 1.8-fold higher $k/A_{685}$ value compared with DPc/m, respectively.

Regarding the oxygen consumption amount, the relative change in $pO_2$ of DPc reached plateau after 100 s of photoirradiation (Fig. 4A), resulting in the lowest oxygen consumption amount after 1000 s of irradiation among photosensitizing agents (Table 3). In Fig. 4B, the
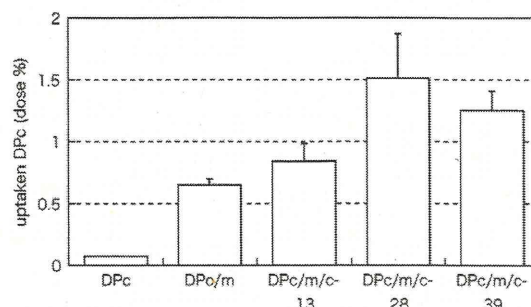
**Fig. 3.** Cellular uptake of ¹²⁵I-labeled DPc, DPc/m and DPc/m/c in A549 cells. Error bars in the graph represent standard deviation ($n = 3$).

linear line of initial gradients of $\ln([O_2]_t/[O_2]_{initial})$ (dotted line) of DPc was greatly apart from the actual measurement (solid line) after 20 s, suggesting early and irradiation-dependent decrease in the oxygen consumption efficiency of DPc. In contrast, the relative change in $pO_2$ of DPc/m constantly decreased despite the lowest k value (Fig. 4A), resulting in a higher oxygen consumption amount after 1000 s compared with DPc (Table 3). In Fig. 4B, the linear line of initial gradients of $\ln([O_2]_t/[O_2]_{initial})$ (dotted line) of DPc/m corresponded to the actual measurement (solid line) until 50 s and the subsequent difference between dotted and solid lines was also smaller than that of DPc, suggesting the sustained oxygen consumption compared with DPc. The DPc/m/c showed continuous oxygen consumption with higher k values than DPc/m, thereby achieving remarkably high oxygen consumption amount after 1000 s beyond DPc and DPc/m (Table 3). The oxygen consumption amount of DPc/m/c increased with an increase in the IM substitution degree of PEG-PLys(IM). These results are consistent with the results in Fig. 4B: the linear line of initial gradients of $\ln([O_2]_t/[O_2]_{initial})$ (dotted line) of DPc/m/c got closer to the actual measurement (solid line) as the IM substitution degree increased.
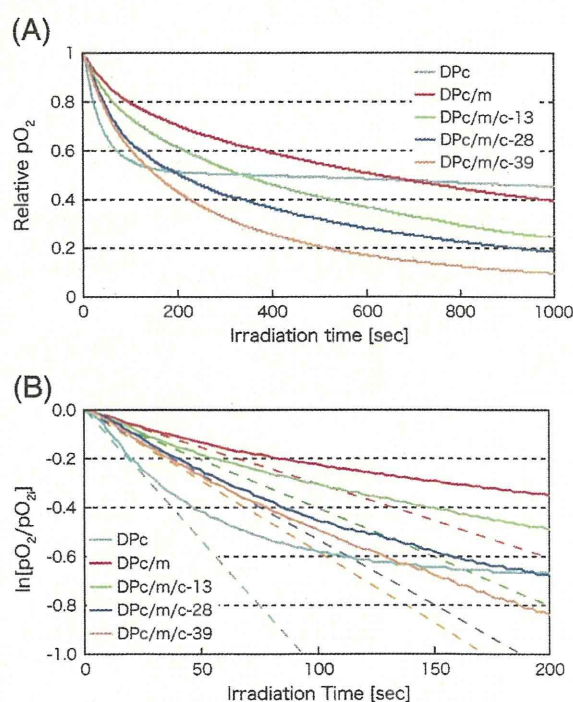
**Fig. 4.** Relative oxygen partial pressure change (A) and logarithmic decay of $pO_2$ (B) in 10 mM phosphate buffered solution (pH 7.4) containing 10% FBS with 13.4 μM DPc, DPc/m and DPc/m/c after the photoirradiation.

**Table 2**
*In vitro* cytotoxicity of photosensitizing agents after photoirradiation using halogen lamp.

| Photoirradiation condition | | IC₅₀ (μM) [a] of photosensitizing agent | | | | |
|---|---|---|---|---|---|---|
| Time (min) | Fluence (J/cm²) | DPc | DPc/m | DPc/m/c-13 | DPc/m/c-28 | DPc/m/c-39 |
| 0 | 0 | >20 | >20 | >20 | >20 | >20 |
| 15 | 2.7 | >20 | 5.0 | 1.0 | 1.0 | 1.0 |
| 30 | 5.4 | >20 | 4.0 | 0.20 | 0.20 | 0.80 |
| 45 | 8.1 | 10 | 2.0 | 0.08 | 0.10 | 0.50 |
| 60 | 10.8 | 8.0 | 0.80 | 0.05 | 0.07 | 0.40 |

[a] 50% cell growth-inhibitory concentration.

**Table 3**
k value (efficiency of the ROS production), oxygen consumption amount after 1000 s of laser irradiation and absorbance spectra at 685 nm (laser wavelength).

| Sample | k value | Oxygen consumption amount | Absorbance at 685 nm | $k/A_{685}$ |
|--------|---------|---------------------------|----------------------|-------------|
| DPc | 0.0096 | 55% | 0.46 | 0.021 |
| DPc/m | 0.0028 | 61% | 0.32 | 0.0088 |
| DPc/m/c-13 | 0.0040 | 75% | 0.33 | 0.012 |
| DPc/m/c-28 | 0.0053 | 82% | 0.34 | 0.016 |
| DPc/m/c-39 | 0.0058 | 91% | 0.36 | 0.016 |

### 3.6. Photobleaching effect

In spite of the highest efficiency of the ROS production, DPc showed the lowest oxygen consumption as summarized in the Table 3. The photobleaching of DPc may be responsible for this effect. To evaluate the photobleaching effect, we measured the absorbance at Q-band peak of DPc every 5 min upon laser irradiation in the media solution containing 10% FBS under the condition saturated with argon gas or oxygen gas. In the saturated oxygen gas condition, the relative absorbance of DPc decreased to 0.51 after 15 min of photoirradiation which is much lower than DPc/m and DPc/m/c [Fig. 5(A)]. In contrast, both DPc/m and DPc/m/c showed the relative absorbance of 0.81–0.85 after 15 min photoirradiation. These results suggest that the micellar formulation might reduce the photobleaching of DPc in the saturated oxygen gas condition. On the other hand, in the saturated argon gas condition [Fig. 5(B)], the relative absorbance of DPc/m/c was kept to be 0.94–0.95 after 15 min photoirradiation, whereas that of DPc/m decreased to 0.82, the value similar to the condition with saturated oxygen. These results suggest that introduction of disulfide cross-linkings might protect the DPc incorporated in the micelle from the photobleaching in the absence of molecular oxygen.

### 3.7. Measurement of ROS production in living cells

In the previous paper, we reported that DPc/m might induce photodamage to the mitochondria and thus affect their functions [9]. In the present study, we observed the fluorescence of MitoSOX Red after photoirradiation to evaluate the ROS production in living cells. As shown in confocal images (Fig. 6A) and quantitative data of mean fluorescent intensity (Fig. 6B), DPc/m-treated cells exhibited stronger fluorescence of MitoSOX Red compared to DPc-treated cells. DPc/m/c-treated cells showed further increase in fluorescence intensity as the IM substitution degree increased to 28%. However, the fluorescence of MitoSOX Red was diminished in the DPc/m/c-39-treated cells. These results suggest that the optimal IM substitution degree might exist for the enhancement of intracellular ROS production by DPc-loaded polymeric micelles.

### 4. Discussion

Drug delivery systems (DDS) have been proposed as an important and effective method in photodynamic therapy (PDT) because they improve the accumulation of the PSs in cancer tissue [4,10,12,13]. Additionally, the ability of PSs to produce ROS effectively is also an essential point of view in PDT. However, PSs generally have large π-conjugation domains and hydrophobic characteristics that easily form aggregates and cause a self-quenching effect of the excited state in aqueous medium. Especially, incorporation into nanocarriers such as liposomes and polymeric micelles can increase the possibility of interaction between PSs, leading to a significant decrease in the ROS production due to the self-quenching effect [28].

To prevent the self-quenching of PSs in nanocarriers, the third-generation dendrimer porphyrin with 32 carboxyl groups on the
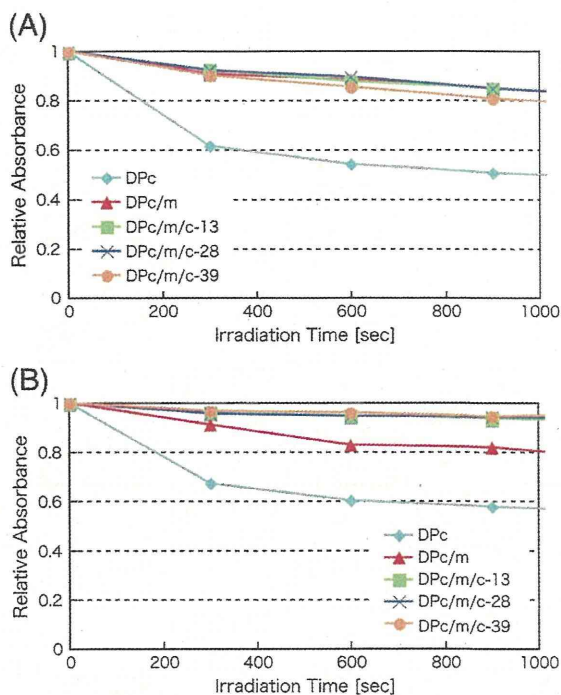


**Fig. 5.** Relative absorbance change of DPc, DPc/m and DPc/m/c-13, -28 and -39 after photoirradiation in the medium saturated with $O_2$ gas (A) and saturated Ar gas (B). Absorbance was recorded from 500 to 800 nm.

periphery (DP) have been developed in our previous study [7,27–29]. The large dendritic wedges of DP prevent the self-quenching effect of DPs in the polyion complex micelle. In the case of dendrimer phthalocyanine (DPc), however, the third-generation dendrimer showed no PDT effect (data not shown), thus we utilized a second-generation dendrimer. The structure of second-generation dendrimer phthalocyanine is relatively planar, thus it cannot completely prevent the self-quenching at high concentrations. From the UV–vis absorption spectra (Fig. 2), we observed that the absorbance decreased at 685 nm (monomeric state) and increased at 630 nm (aggregated state) by incorporation of DPc into the micelle as previously reported [8], suggesting the self-quenching of DPc in the micellar core. Nevertheless, it is intriguing that the DPc-loaded PIC micelle (DPc/m) still showed 10-fold higher photocytotoxicity than DPc (Table 2).

One of the reasons for the enhanced photocytotoxicity of DPc/m is a 9-fold increase in the cellular uptake of DPc by the incorporation into the micelle as shown in Fig. 3. In addition to the cellular uptake, we investigated the photochemical properties of DPc/m under the diluted condition to clarify the enhanced photocytotoxicity. In the measurement of oxygen consumption, the k value [initial gradients of $\ln([O_2]_t/[O_2]_{initial})$ in Fig. 4B], which are correlated with the efficiency of the ROS production, decreased to about 1/3 by incorporation of DPc into the micelle. Also, the $k/A_{685}$ values, which are correlated with the quantum yield of ROS production, decreased by incorporation of DPc into the micelle. These results strongly suggest the self-quenching of DPc in the micellar core, as predicted by the decrease at 685 nm (monomeric state) and increase at 630 nm (aggregated state) in the absorbance peak of the DPc/m compared to DPc shown in Fig. 2. However, the oxygen consumption amount of DPc/m after 1000 s of photoirradiation was higher than that of DPc (Table 3), because the relative $pO_2$ change of DPc reached the plateau after 100 s of photoirradiation. Therefore, DPc/m might more effectively produced ROS in cumulative value than DPc in spite of its decreased quantum yield of the ROS production. To explain this phenomenon, we have
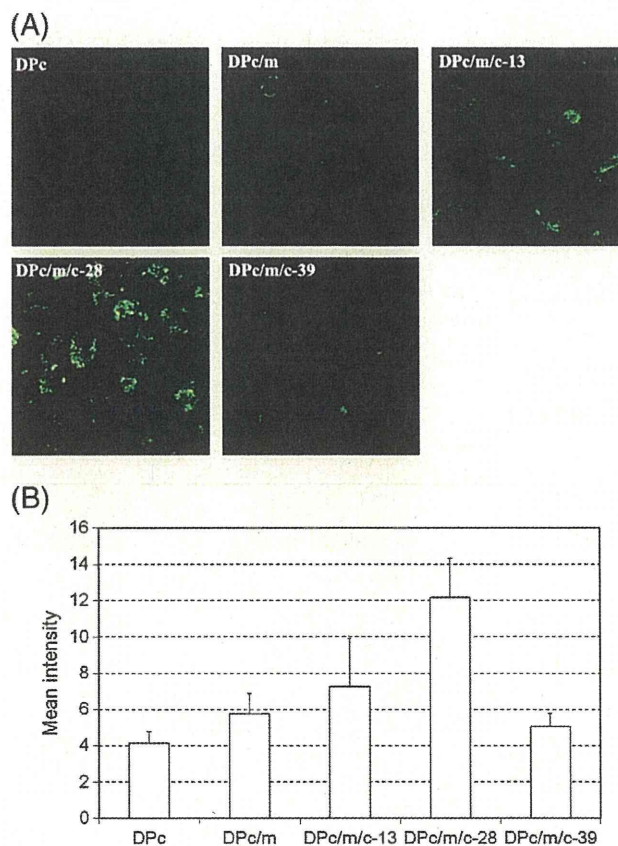
**Fig. 6.** Fluorescence of MitoSOX Red in the DPc, DPc/m, and DPc/m/c-treated A549 cells after 15 min photoirradiation.

evaluated the photobleaching effect of DPc in the solution containing 10% FBS under saturated oxygen gas condition (Fig. 5A). It was revealed that photobleaching of DPc can be diminished by its incorporation into the micelle. In order to investigate the photobleaching of DPc in the absence of molecular oxygen, the same experiment under saturated argon gas condition was performed. As a result, similar tendency was observed under both saturated oxygen and argon gas conditions (Fig. 5B). As described in the Introduction, there are two mechanisms in the photochemical reactions of PSs. The type I reaction directly damages PSs due to the proton/electron transfer to the acceptors such as molecular oxygen and biomolecules, whereas the type II reaction through the energy transfer process from the triplet excited state of PSs to molecular oxygen in the triplet ground state does not damage the PSs. In the Fig. 5B, DPc exhibited considerable photobleaching effect in the absence of oxygen molecules, suggesting that DPc was damaged due to the proton/electron transfer to serum proteins as an acceptor (type I reaction). DPc/m showed less photobleaching level compared to DPc in the saturated argon gas condition, suggesting the photobleaching process due to the proton/electron transfer to serum proteins can be diminished by incorporation of DPc into the micelle. That is, the core-shell type micellar structure might sterically prevent the interaction of serum proteins with DPc in the micellar core, thus protecting DPc from the photobleaching (Fig. 7). We have further developed disulfide cross-linked DPc-loaded micelle (DPc/m/c) with the aim to improve the stability in biological media. In this study, we found that introduction of disulfide crosslinking further enhanced the photocytotoxicity; DPc/m/c-13 and'DPc/m/c-28 achieved more than 10-fold greater photocytotoxicity than DPc/m. In Fig. 3, DPc/m/c-13 and DPc/m/c-28 showed 1.3 and 2.3-fold higher cellular uptake than DPc, which could not fully explain a 10-fold increase in photocytotoxicity.

Therefore, we investigated the photochemical properties of DPc/m/c. First, the UV–vis spectra showed that the absorbance peak at 685 nm (monomeric state) increased as the thiol substitution degree increased (Fig. 2, Table 3). In agreement to this result, the k and $k/A_{685}$ values increased with the thiol substitution degree (Table 3). Thus, introduction of the disulfide crosslinking into the micellar core might improve the quantum yield of ROS production of PSs. It is assumed that the disulfide crosslinking of the micellar core may restrict the movement of DPc, therefore reducing the interactions between DPc molecules in the core. Meanwhile, the oxygen consumption amount considerably increased with the thiol substitution degree (Table 3). In the photobleaching experiment, similar photobleaching levels were observed between DPc/m and DPc/m/c under saturated oxygen gas condition (Fig. 5A); however, DPc/m/c displayed less photobleaching than DPc/m under saturated argon gas condition (Fig. 5B). These results suggest that disulfide crosslinked micelle might prevent the type I photochemical reaction with serum proteins as the acceptor. Generally, PIC micelles possess an equilibrium between unimers and multimolecular micellar structures. Indeed, the ultracentrifugation experiment revealed that 36% of DPc exists as unimers in 5 times diluted non-crosslinked DPc/m solution, whereas unimers were not detected in all the crosslinked DPc/m at the same experimental condition (See Supporting Information, Figure S3). It is most likely that the introduction of the disulfide crosslinking might improve the stability of the micellar structure against dilution. As illustrated in Fig. 7B, DPc in the unimer components could easily interact with serum proteins and photobleach due to imperfect shielding by PEG. This hypothesis is consistent with our observation that, even in the absence of oxygen molecules, DPc/m showed 15–19% decrease in the relative absorbance after 15 min photoirradiation (Fig. 5B). Possibly, the presence of serum may destabilize the multimolecular structure of
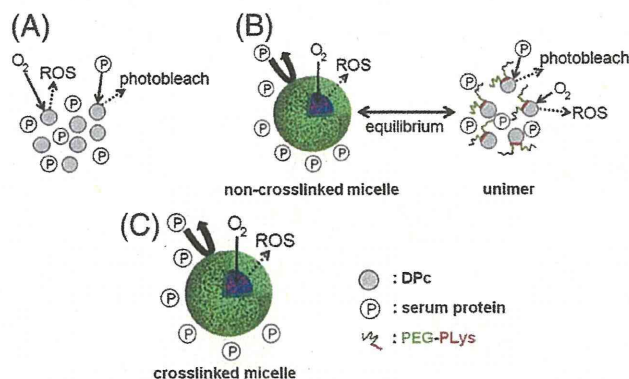
**Fig. 7.** Hypothetic illustration of interaction of DPc with $O_2$ and serum proteins in DPc (A), DPc/m (B) and DPc/m/c (C).

the non-crosslinked micelles, which may facilitate the photobleaching as seen in Fig. 5B. In contrast, DPc/m/c might retain the stabilized multimolecular structure without unimers even under the diluted condition with serum proteins. This mechanism is consistent with the result that the DPc/m/c can prevent photobleaching process caused by type I photochemical reactions with serum proteins as illustrated in Fig. 7C. Worth mentioning is that under the saturated oxygen gas condition, DPc/m and DPc/m/c showed similar photobleaching levels, suggesting that oxygen molecules can react with the micellar core via the type I and/or type II photochemical reactions. In other words, disulfide crosslinking in the micellar core could prevent undesirable type I photochemical reaction with serum proteins leading to photobleaching of PSs but could not compromise the photochemical reactions involving oxygen molecules essential to the PDT effect.

As aforementioned, introduction of the disulfide crosslinking has been revealed to improve the cellular uptake and the efficiency of oxygen consumption of the DPc-loaded micelle as shown in Figs. 3 and 4A, respectively. The thiol substitution degree of DPc/m/c was correlated with their cellular uptake and the efficiency of oxygen consumption. However, the optimal thiol substitution degree existed for the *in vitro* photocytotoxicity, i.e., DPc/m/c-13 and DPc/m/c-28 achieved more than 10-fold greater photocytotoxicity than DPc/m, whereas DPc/m/c-39 showed only 2-fold higher photocytotoxicity than DPc/m. Therefore, we evaluated the ROS production in living cells by using MitoSOX Red. As a result, DPc/m/c showed increased fluorescence intensity of MitoSOX Red as the IM substitution degree increased to 28%. However, the fluorescence of MitoSOX Red was diminished when the IM substitution degree was 39% (Fig. 6). We previously reported that DPc-loaded micelles are internalized through the endocytic pathway and translocated from the endo-/lysosomes to the cytoplasm through the photochemical disruption of the endo-/lysosomal membranes, followed by photodamage to the mitochondria [9]. In the present study, the photocytotoxicity study (Table 2) revealed that DPc/m/c-13 and -28 showed more than 10-fold increase in the PDT effect when the irradiation time increased from 15 min to 60 min; however, DPc/m/c-39 showed only 2.5-fold increase in the PDT effect. We previously reported that disulfide-crosslinked polyion complex micelles incorporating plasmid DNA (pDNA) with excessive thiol groups (thiol substitution ratio: 37%) showed decreased pDNA release efficiency against the counter polyanion exchange under the reductive conditions, thereby showing a significant decrease in the gene transfection efficiency [20], since an increase in the disulfide crosslinking density in the micellar core should decrease the mobility of polymer chains in the core to enhance the crosslinking stability under reductive environment. Therefore, we assume that the reduced photocytotoxity of DPc/m/c-39 might be attributed to this over-stabilization effect in the core structures. In other words, photo-irradiation might induce structural change of DPc/m/c-13 and -28, which might be essential for endosomal escape and photodamage to

mitochondria. Regarding the detailed intracellular behaviors of DPc-loaded micelles, further studied should be performed.

## 5. Conclusion

Effective photochemical reactions should be an important factor in realization of enhanced PDT. In the photochemical reactions, PSs react with oxygen molecules, leading to production of ROS, while the reaction with biomolecules such as serum proteins results in inactivation of PSs by photobleaching. In this study, we demonstrated that the incorporation of DPc into the micelle and introduction of disulfide crosslinking into the micellar core could prevent unfavorable photochemical reaction with the serum proteins without compromising photochemical reactions involving oxygen molecules, leading to remarkably enhanced PDT. Until now, there have been a number of studies regarding the development of nanocarriers for the delivery of PSs, and those studies have focused only on improvement of biodistribution of PSs. In this study, we revealed that, in addition to *in vivo* PS delivery, micellar nanocarriers can alter the photochemical reactions to more favorable mechanisms, which further improved the PDT effect. Our findings should have a great impact and be useful for designing nanocarriers for the delivery of PSs.

## Appendix A. Supplementary data

Supplementary data to this article can be found online at doi:10.1016/j.jconrel.2011.06.019.

## References

[1] D.E.J.G.J. Dolmans, D. Fukumura, R.K. Jain, Photodynamic therapy for cancer, Nat. Rev. Cancer 3 (2003) 380–387.
[2] T.J. Dougherty, C.J. Gomer, B.W. Henderson, G. Jori, D. Kessel, M. Korbelik, J. Moan, Q. Peng, Photodynamic therapy, J. Natl. Cancer Inst. 90 (1998) 889–905.
[3] A.M.R. Fisher, A.L. Mulphree, C.J. Gomer, Clinical and preclinical photodynamic therapy, Laser. Surg. Med. 17 (1996) 2–32.
[4] G. Palumbo, Photodynamic therapy and cancer: a brief sightseeing tour, Expert Opin. Drug Deliv. 4 (2007) 131–148.
[5] A. Juarranz, P. Jaén, F. Sanz-Rodríguez, J. Cusvas, S. González, Photodynamic therapy of cancer: basic principles and applications, Clin. Transl. Oncol. 10 (2008) 148–154.

[6] C.J.F. Rijcken, J.W. Hofman, F. Zeeland, W.E. Hennink, C.F. Nostrum, Photosensitizer-loaded biodegradable polymeric micelles: preparation, characterization and *in vitro* PDT efficacy, J. Control. Release 124 (2007) 144–153.

[7] H.R. Stapert, N. Nishiyama, D.L. Jiang, T. Aida, K. Kataoka, Polyion complex micelles encapsulating light-harvesting ionic dendrimer zinc porphyrins, Langmuir 16 (2000) 8182–8188.

[8] W.D. Jang, Y. Nakagishi, N. Nishiyama, S. Kawauchi, Y. Morimoto, M. Kikuchi, K. Kataoka, Polyion complex micelles for photodynamic therapy: incorporation of dendritic photosensitizer excitable at long wavelength relevant to improved tissue-penetrating property, J. Control. Release 113 (2006) 73–79.

[9] N. Nishiyama, Y. Nakagishi, Y. Morimoto, P.S. Lai, K. Miyazaki, K. Urano, S. Horie, M. Kumagai, S. Fukushima, Y. Cheng, W.D. Jang, M. Kikuchi, K. Kataoka, Enhanced photodynamic cancer treatment by supramolecular nanocarriers charged with dendrimer phthalocyanine, J. Control. Release 133 (2009) 245–251.

[10] N. Nishiyama, Y. Morimoto, W.D. Jang, K. Kataoka, Design and development of dendrimer photosensitizer-incorporated polymeric micelles for enhanced photodynamic therapy, Adv. Drug Deliv. Rev. 61 (2009) 327–338.

[11] N. Nishiyama, W.D. Jang, K. Kataoka, Supramolecular nanocarriers integrated with dendrimers encapsulating photosensitizers for effective photodynamic therapy and photochemical gene delivery, New J. Chem. 31 (2007) 1074–1082.

[12] A.S.L. Derycke, P.A.M. de White, Liposomes for photodynamic therapy, Adv. Drug Deliv. Rev. 56 (2004) 17–30.

[13] C.F. van Nostrum, Polymeric micelles to deliver photosensitizers for photodynamic therapy, Adv. Drug Deliv. Rev. 56 (2004) 9–16.

[14] D. Le Garrec, J. Taillefer, J.E. Van Lier, V. Lenaerts, J.-C. Leroux, Optimizing pH responsive polymeric micelles for drug delivery in a cancer photodynamic therapy model, J. Drug Target. 10 (2002) 429–437.

[15] Y. Matsumura, H. Maeda, A new concept for macromolecular therapeutics in cancer chemotherapy: mechanism of tumoritropic accumulation of proteins and the antitumor agent SMANCS, Cancer Res. 46 (1986) 6387–6392.

[16] K. Miyata, R.J. Christie, K. Kataoka, Polymeric micelles for nano-scale drug delivery, React. Funct. Polym. 71 (2011) 227–234.

[17] S. Bauhunber, C. Hozsa, M. Breunig, A. Göpferich, Delivery of nucleic acids via disulfide-based carrier systems, Adv. Mater. 21 (2009) 32–33.

[18] G.D. Fasman, M. Idelson, E.R. Blout, The synthesis and conformation of high molecular weight poly-ε-carbobenzyloxy-L-lysine and poly-L-lysine·HCl, J. Am. Chem. Soc. 83 (1961) 709–712.

[19] S. Matsumoto, R.J. Christie, N. Nishiyama, K. Miyata, A. Ishii, M. Oba, H. Koyama, Y. Yamasaki, K. Kataoka, Environment-responsive block copolymer micelles with a disulfide cross-linked core for enhanced siRNA delivery, Biomacromolecules 10 (2009) 119–127.

[20] K. Miyata, Y. Kakizawa, N. Nishiyama, A. Harada, Y. Yamasaki, H. Koyama, K. Kataoka, Block catiomer polyplexes with regulated densities of charge and disulfide cross-linking directed to enhance gene expression, J. Am. Chem. Soc. 126 (2004) 2355–2361.

[21] P.W. Riddles, R.L. Blakeley, B. Zerner, Ellman's reagent: 5,5-dithiobis(2-nitrobenzoic acid) – a reexamination, Anal. Biochem. 94 (1979) 75–81.

[22] F.C. Greenwood, M.W. Hunter, J.S. Glover, The preparation of ^{131}I-labelled human growth hormone of high specific radioactivity, Biochem. J. 89 (1963) 114–123.

[23] R.M. Cory, J.B. Cotner, K. McNeill, Quantifying interactions between singlet oxygen and aquatic fulvic acids, Environ. Sci. Technol. 43 (2009) 718–723.

[24] S. Subbiah, R. Mokaya, Synthesis of transparent and ordered mesoporous silica monolithic films embedded with monomeric zinc phthalocyanine dye, Chem. Commun. (2003) 860–861.

[25] M.E. Wieder, D.C. Hone, M.J. Cook, M.M. Handsley, J. Gavrilovicb, D.A. Russell, Intracellular photodynamic therapy with photosensitizer-nanoparticle conjugates: cancer therapy using a 'Trojan horse', Photochem. Photobiol. Sci. 5 (2006) 727–734.

[26] S. Wei, J. Zhou, D. Huang, X. Wang, B. Zhang, J. Shen, Synthesis and Type I/Type II photosensitizing properties of a novel amphiphilic zinc phthalocyanine, Dye. Pigment. 71 (2006) 61–67.

[27] W.-D. Jang, N. Nishiyama, G.D. Zhang, A. Harada, D.-L. Jiang, S. Kawauci, Y. Morimoto, M. Kikuchi, H. Koyama, T. Aida, K. Kataoka, Supramolecular nanocarrier of anionic dendrimer porphyrins with cationic block copolymers modified with polyethylene glycol to enhance intracellular photodynamic efficacy, Angew. Chem. Int. Ed. 44 (2005) 419–423.

[28] Y. Li, W.-D. Jang, N. Nishiyama, A. Kishimura, S. Kawauchi, Y. Morimoto, S. Miake, T. Yamashita, M. Kikuchi, T. Aida, K. Kataoka, Dendrimer generation effects on photodynamic efficacy of dendrimer porphyrins and dendrimer-loaded supramolecular nanocarriers, Chem. Mater. 19 (2007) 5557–5562.

[29] N. Nishiyama, H.R. Stapert, G.-D. Zhang, D. Takasu, D.-L. Jiang, T. Nagano, T. Aida, K. Kataoka, Light-harvesting ionic dendrimer porphyrins as new photosensitizers for photodynamic therapy, Bioconjugate Chem. 14 (2003) 58–66.

# Odd—Even Effect of Repeating Aminoethylene Units in the Side Chain of N-Substituted Polyaspartamides on Gene Transfection Profiles

Hirokuni Uchida,[†] Kanjiro Miyata,[§] Makoto Oba,[∥] Takehiko Ishii,[†] Tomoya Suma,[†] Keiji Itaka,[§] Nobuhiro Nishiyama,[§] and Kazunori Kataoka*,[†,§,‡]

[†]Department of Bioengineering and [‡]Department of Materials Engineering, Graduate School of Engineering, The University of Tokyo, 7-3-1 Hongo, Bunkyo, Tokyo 113-8656, Japan

[§]Center for Disease Biology and Integrative Medicine, Graduate School of Medicine, The University of Tokyo, 7-3-1 Hongo, Bunkyo, Tokyo 113-0033, Japan

[∥]Department of Clinical Vascular Regeneration, Graduate School of Medicine, The University of Tokyo, 7-3-1 Hongo, Bunkyo, Tokyo 113-8655, Japan

Ⓢ Supporting Information

**ABSTRACT:** A series of the N-substituted polyaspartamides possessing repeating aminoethylene units in the side chain was prepared in this study to identify polyplexes with effective endosomal escape and low cytotoxicity. All cationic N-substituted polyaspartamides showed appreciably lower cytotoxicity than that of commercial transfection reagents. Interestingly, a distinctive odd—even effect of the repeating aminoethylene units in the polymer side chain on the efficiencies of endosomal escape and transfection to several cell lines was observed. The polyplexes from the polymers with an even number of repeating aminoethylene units (PA-Es) achieved an order of magnitude higher transfection efficiency, without marked cytotoxicity, than those of the polymers with an odd number of repeating aminoethylene units (PA-Os). This odd—even effect agreed well with the buffering capacity of these polymers as well as their capability to disrupt membrane integrity selectively at endosomal pH, leading to highly effective endosomal escape of the PA-E polyplexes. Furthermore, the formation of a polyvalent charged array with precise spacing between protonated amino groups in the polymer side chain was shown to be essential for effective disruption of the endosomal membrane, thus facilitating transport of the polyplex into the cytoplasm. These data provide useful knowledge for designing polycations to construct safe and efficient nonviral gene carriers.
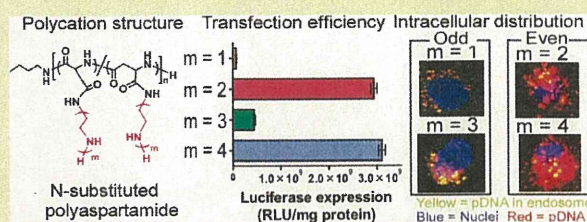
# INTRODUCTION

Gene therapy has received considerable attention because of its significant potential to treat intractable diseases; however, the development of safe and efficient carriers of plasmid DNA (pDNA) remains a critical issue.[1,2] Among pDNA carriers, polyion complexes (PICs) formed between negatively charged DNA and polycations, which are termed "polyplexes", have been extensively studied.[3-8] Such polyplexes are required to stably deliver pDNA to the nuclei in the target cells. However, the most critical issue affecting the trafficking of polyplexes is the inefficient translocation from the endosomes to the cytoplasm after internalization through the endocytosis.[9] Hence, considerable efforts have been devoted to the development of polycations with potent endosomal escape ability.[10-15] However, such polycations often cause severe cytotoxicity.[16] Therefore, the fine-tuning the chemical structures of polycations to enhance their endosomal escape ability while cytotoxicity is reduced is a major key in designing polyplexes; this proves to be a challenge with respect to various fields of chemistry.

Linear polyethylenimine (linear PEI) is one of the most widely used polycations possessing potent endosomal escape ability.[17-20]

Indeed, linear PEI polyplexes have been examined in several disease models to evaluate their clinical applications.[21] Linear PEI consists of repeating aminoethylene units and features a relatively low $pK_a$.[22] Hence, the protonation degree of linear PEI increases when pH decreases from the extracellular pH (~7.4) to the endosomal pH (~5.5). This facilitates the endosomal escape of linear PEI polyplexes because of endosomal disruption caused by increased osmotic pressure in the endosome (the so-called proton sponge effect[12,17]) and/or perturbation of the endosomal membrane caused by a direct interaction with polycations.[23-26] Thus, linear PEI exhibits a relatively high transfection efficiency but consequently induces considerable cytotoxicity because of interactions with biomolecules including the plasma membrane.[16,27] In order to solve this cytotoxicity problem, we have truncated a defined number of repeating aminoethylene units and introduced them into the side chain of the N-substituted polyaspartamides to obtain fine-tuned polycations achieving efficient gene transfection but reduced cytotoxicity. In our previous study,

**Scheme 1.** Synthesis of PAsp(EDA), PAsp(DET), PAsp(TET), and PAsp(TEP) by Aminolysis of PBLA



$R_m = -(CH_2CH_2N)_m^H -H$

m = 1: PAsp(EDA), m = 2: PAsp(DET), m = 3: PAsp(TET), m = 4: PAsp(TEP)
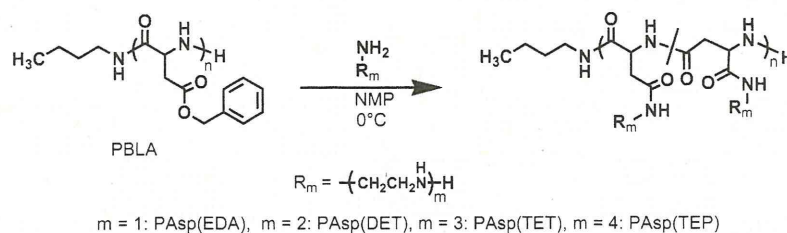
poly{$N$-[$N'$-(2-aminoethyl)-2-aminoethyl]aspartamide} possessing two repeating aminoethylene units [$-(CH_2-CH_2-NH)_2-H$] was synthesized by the introduction of diethylenetriamine (DET) (bis(2-aminoethyl)amine) [PAsp(DET)] into the side chain of the N-substituted polyaspartamide.[28] PAsp(DET) showed minimal membrane destabilizing ability with a mono-protonated side chain at pH 7.4 but a potent membrane destabilizing effect with a diprotonated side chain at pH 5.5. Thus, PAsp(DET) is assumed to selectively damage the endosomal membrane, thus enabling less toxic gene transfer in various cells including fragile primary culture cells.[26] Furthermore, the in vivo efficacy of gene transfer using PAsp(DET) has been demonstrated in several disease models.[29,30]

These studies motivated us to further investigate the relationship between the protonation behavior and biological properties of the N-substituted polyaspartamides possessing repeating aminoethylene units in the side chain. We expect such studies to provide useful knowledge for designing polycations that are safe and efficient nonviral gene carriers. Therefore, in this study, we examined various N-substituted polyaspartamides possessing different numbers of repeating aminoethylene units in the side chain and evaluated the relationship between their protonated states at pH 7.4 and 5.5 and their biological properties such as the hemolytic activity, cytotoxicity, endosomal escape ability, and transfection efficiency. Interestingly, a distinctive odd—even effect associated with the number of aminoethylene units was observed on the efficiencies of endosomal escape and in vitro transfection. The polyplexes from the N-substituted polyaspartamides possessing even-numbered repeating aminoethylene units (PA-Es) achieved transfection efficiencies, without marked cytotoxicity, that were an order of magnitude higher than those from the N-substituted polyaspartamides possessing odd-numbered repeating aminoethylene units (PA-Os). The mechanism for endosomal escape of these N-substituted polyaspartamide polyplexes was examined in detail to explain this interesting odd—even effect.

## ■ RESULTS

**Synthesis and Characterization of N-Substituted Polyaspartamides.** Introduction of repeating aminoethylene units into the poly($\beta$-benzyl-L-aspartate) (PBLA) side chain was performed by the aminolysis reaction of PBLA with ethylenediamine (EDA), diethylenetriamine (DET), triethylenetetramine (TET), or tetraethylenepentamine (TEP), as previously reported,[31] and we synthesized poly[$N$-(2-aminoethyl)aspartamide] [PAsp(EDA)], PAsp(DET), poly($N$-{$N'$-[$N''$-(2-aminoethyl)-2-aminoethyl]-2-aminoethyl}aspartamide) [PAsp(TET)], and poly-[$N$-($N'$-{$N''$-[$N'''$-(2-aminoethyl)-2-aminoethyl]-2-aminoethyl}-2-aminoethyl)aspartamide] [PAsp(TEP)] (Scheme 1). It is noteworthy that in this way a series of N-substituted cationic

polyaspartamides, with the same polymerization degree and molecular weight distribution, was readily obtained.[32] Each N-substituted cationic polyaspartamide is abbreviated as PAsp-(R), in which R denotes the abbreviation of the amines substituted in the side chain. The quantitative aminolysis of the side chain was confirmed from the peak intensity ratio of the protons from the methyl group at the $\alpha$-chain end of the polymer ($CH_3CH_2CH_2CH_2-$, $\delta = 0.9$ ppm) to all the methylene protons in the side chains ($\delta = 2.7-3.6$ ppm) in the $^1H$ NMR spectra (Figure 1).

**pH-Dependent Change in the Degree of Protonation ($\alpha$) of Amino Groups in the Side Chain of N-Substituted Polyaspartamides.** In order to estimate the protonation states of the amino groups in the side chain of the N-substituted polyaspartamide (hereafter, the polymer), potentiometric titration was performed in the pH range 1.2–11.5 in a 150 mM NaCl solution at 37 °C. The resultant titration curves were converted to differential curves to determine each neutralization point (data not shown). The total molar amount of consumed NaOH in the titration of PAsp(EDA) and PAsp(DET) corresponded well to the residual molar amount of amino groups of each polymer (5 mmol) in the solution, indicating that all the amino groups of the polymer were protonated at the beginning (pH 1.2) and deprotonated at the end (pH 11.5). Accordingly, the degree of protonation ($\alpha$) and p$K$ ($=$pH $+ \log[\alpha/(1-\alpha)]$) were calculated and plotted against pH and $\alpha$, respectively (Figure 2). On the other hand, the molar amount of consumed NaOH for the titration of PAsp(TET) and PAsp(TEP) was substantially lower than the residual molar amount of amino groups in the solution, suggesting that the amino groups in PAsp(TET) and PAsp-(TEP) should not be fully protonated, even at pH 1.2. Thus, the $\alpha$/pH and p$K/\alpha$ curves of these polymers were calculated from the neutralization point in the differential curve and also shown in Figure 2. The change in the degree of protonation between pH 7.4 and 5.5 ($\Delta\alpha$), indicating the buffering capacity, was calculated for each polymer from the values of $\alpha$ at pH 7.4 and 5.5 and is summarized in Table 1. Obviously, PAsp(DET) showed the largest $\Delta\alpha$, followed by PAsp(TEP), PAsp(TET), and PAsp-(EDA). The number of protonated amines in each polymer (NA) at the corresponding pH was also calculated from $\alpha$ and the number of residual amino groups in the polymer by the following equation: NA $= \alpha n \times 102$, where $n$ is the repeating number of aminoethylene units in the polymer side chain and 102 is the averaged polymerization degree. Furthermore, the averaged cationic charge density (CD) of each polymer was defined as the ratio of the NA to the number-averaged molecular weight ($M_n$) of the polymers (Table 1). The p$K_a$ values for each protonation step were determined from the p$K/\alpha$ curves and are summarized in Table 1. Note that the p$K_{a4,TEP}$ value was not determined because the fourth protonation of the residual amino
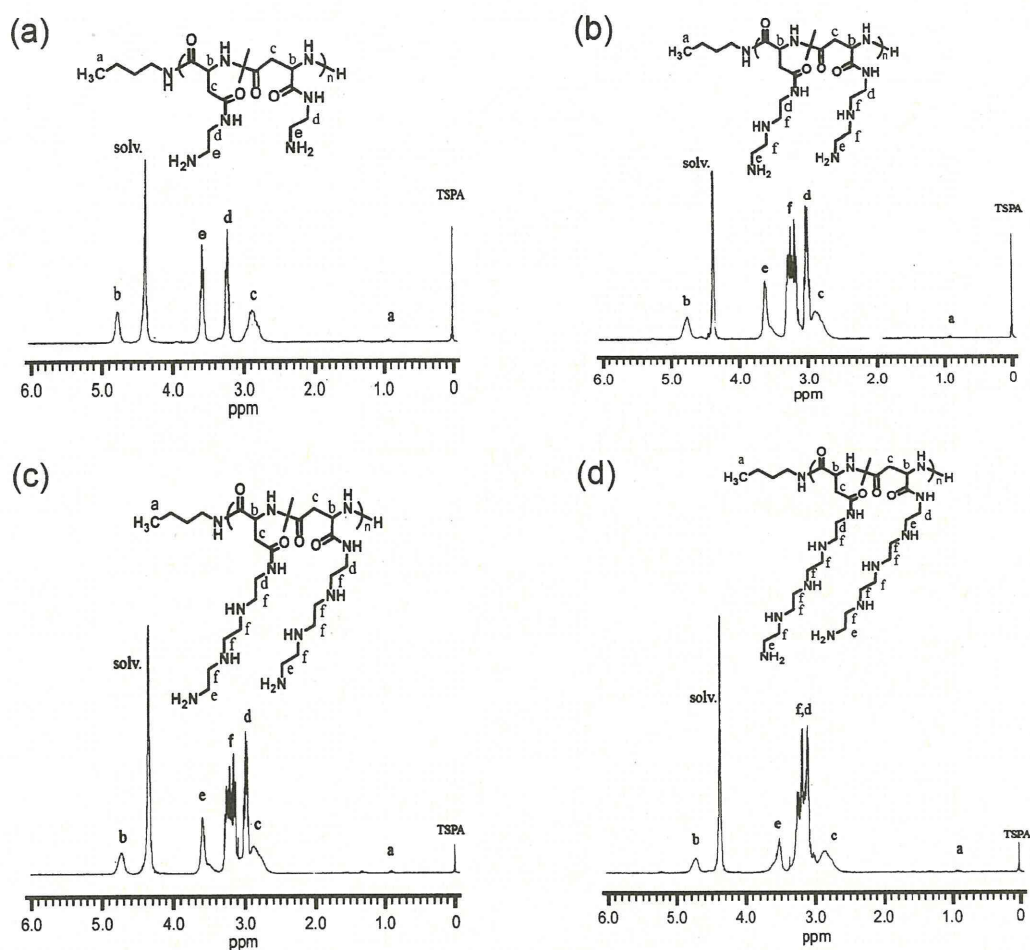
**Figure 1.** $^1$H NMR spectra of (a) PAsp(EDA), (b) PAsp(DET), (c) PAsp(TET), and (d) PAsp(TEP). Solvent, D$_2$O; temperature, 70 °C; polymer concentration, 10 mg/mL.
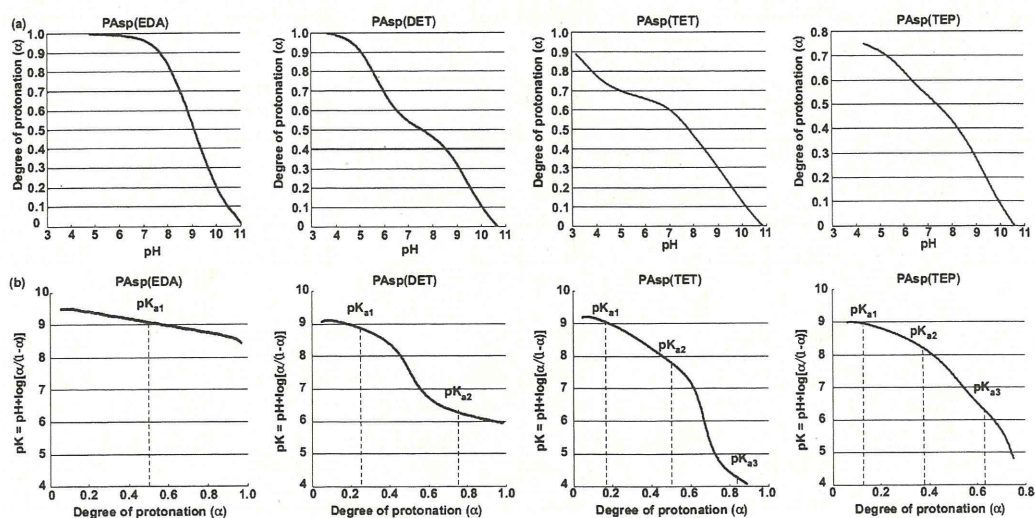


**Figure 2.** (a) $\alpha$/pH curves and (b) pK$_a$/$\alpha$ curves of each N-substituted polyaspartamide in 150 mM NaCl solution at 37 °C.

**Table 1. Physicochemical Parameters of the N-Substituted Polyaspartamides at pH 7.4 and 5.5**

| polymer | $\alpha$ | | | number of protonated amines (NA[a]) | | charge density (CD[b]) | | | | |
|---|---|---|---|---|---|---|---|---|---|---|
| | pH 7.4 | pH 5.5 | $\Delta\alpha$ | pH 7.4 | pH 5.5 | pH 7.4 | pH 5.5 | $pK_{a_1}$ | $pK_{a_2}$ | $pK_{a_3}$ |
| PAsp(EDA) | 0.93 | 0.99 | 0.06 | 94 | 100 | 0.00538 | 0.00621 | 9.0 | | |
| PAsp(DET) | 0.51 | 0.82 | 0.31 | 104 | 167 | 0.00505 | 0.00811 | 8.9 | 6.2 | |
| PAsp(TET) | 0.56 | 0.66 | 0.10 | 171 | 205 | 0.00682 | 0.00817 | 9.1 | 7.8 | 4.3 |
| PAsp(TEP) | 0.49 | 0.68 | 0.17 | 199 | 277 | 0.00673 | 0.00936 | 9.0 | 8.2 | 6.3 |

[a] NA = $\alpha \times$ (the repeating number of aminoethylene units in the polymer side chain) $\times$ (the polymerization degree). [b] The ratio of the NA to the number-averaged molecular weight ($M_n$) of polymers.



$R_m = \left(CH_2CH_2\overset{H}{N}\right)_m H$

m = 1: PAsp(EDA),  m = 2: PAsp(DET)
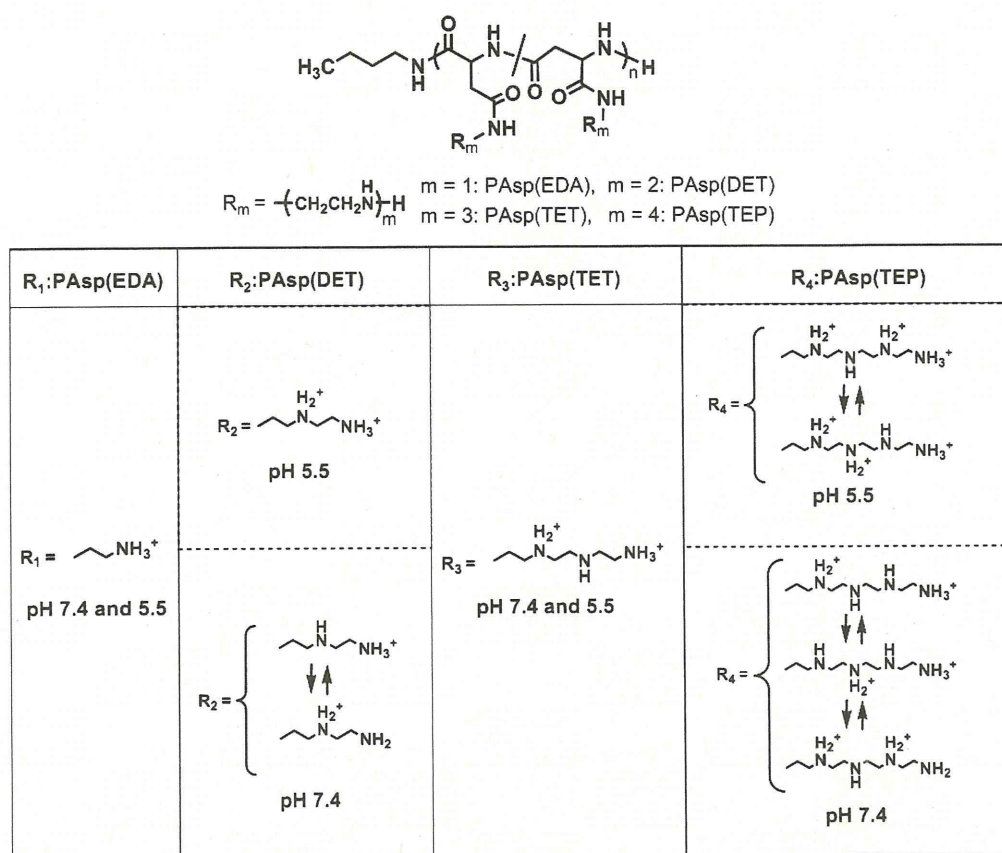m = 3: PAsp(TET),  m = 4: PAsp(TEP)



**Figure 3.** Major protonated structures of amino groups in the side chain of each polyaspartamide at pH 7.4 and 5.5.

groups in PAsp(TEP) was substantially limited, even at pH 1.2. Eventually, the major protonated structures of these polymers under physiological (pH = 7.4) and endosomal (pH = 5.5) conditions were estimated as shown in Figure 3.

**Membrane Destabilizing Activity of N-Substituted Polyaspartamides.** Our previous study revealed that PAsp(DET) disturbs the integrity of cellular membranes selectively at endosomal acidic pH presumably because of the transition of the side chain diamine unit from a monoprotonated to diprotonated state, which enhances the local charge density and facilitates the interaction with cellular membranes.[26] To determine the membrane-destabilizing activities of the N-substituted polyaspartamides as well as linear PEI (ExGen 500), the hemolysis assay was performed by mixing these polymers with murine erythrocytes

at pH 7.4 and 5.5, at which extracellular neutral and endosomal acidic conditions, respectively, were simulated. As shown in Figure 4, ExGen 500 showed a considerably high hemolysis ratio (approximately 30%) at pH 7.4, which may be correlated with its high cytotoxicity. In contrast, all polymers induced substantially low hemolysis (less than 5%) at pH 7.4. Alternatively, at pH 5.5, the polymers possessing even-numbered repeating aminoethylene units [PAsp(DET) and PAsp(TEP)] and ExGen 500 significantly enhanced the hemolytic activity, whereas those possessing odd-numbered repeating units [PAsp(EDA) and PAsp(TET)] showed no significant increase. Thus, a unique odd−even effect of the repeating number of aminoethylene units was clearly observed for the pH-dependent hemolytic activity of a series of N-substituted polyaspartamides. Furthermore, the hemolytic
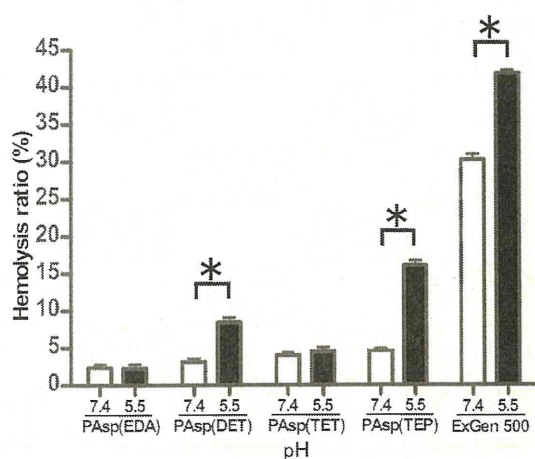
**Figure 4.** Hemolytic activity of PAsp(EDA), PAsp(DET), PAsp(TET), PAsp(TEP), and ExGen 500 ([amine] = 5 mM) against murine erythrocytes at pH 7.4 and 5.5. Results are expressed as mean ± SEM ($N = 4$). *$P < 0.05$.
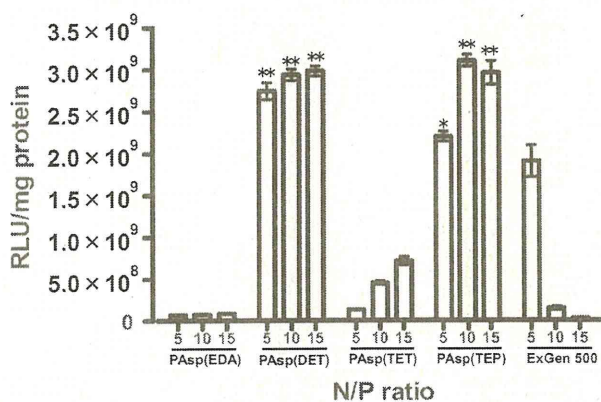


**Figure 5.** In vitro transfection efficiency of PAsp(EDA), PAsp(DET), PAsp(TET), PAsp(TEP), and ExGen 500 polyplexes at varying N/P ratios with Huh-7 cells determined by luciferase assay. Results are expressed as mean ± SEM ($N = 4$). * indicates that polyplexes show a significantly higher transfection efficiency than the PA-Os polyplexes at the same N/P ratio ($P < 0.01$), ** indicates that polyplexes show a significantly higher transfection efficiency than the PA-Os polyplexes at the same N/P ratio ($P < 0.01$) and the ExGen 500 polyplexes at N/P = 5 ($P < 0.05$).

activities of the polyplexes from the N-substituted polyaspartamides and ExGen 500 were determined at N/P = 10, which corresponds to the residual molar ratio of the amino groups in polycations to the phosphate groups in pDNA (Figure 1, Supporting Information). The hemolytic activity of polyplexes showed a similar odd−even effect, indicating that the membrane-destabilizing activity of the polycations was maintained even after the formation of polyplexes.

### Size and ζ-Potential of Polyplexes Prepared from pDNA and N-Substituted Polyaspartamides.
The polyplexes from the N-substituted polyaspartamides were characterized by measuring the ζ-potential and hydrodynamic diameter at pH 7.4 and 37 °C (Figure 2, Supporting Information). At N/P ratios above 4, all polyplexes had a similar size of approximately 100 nm with a
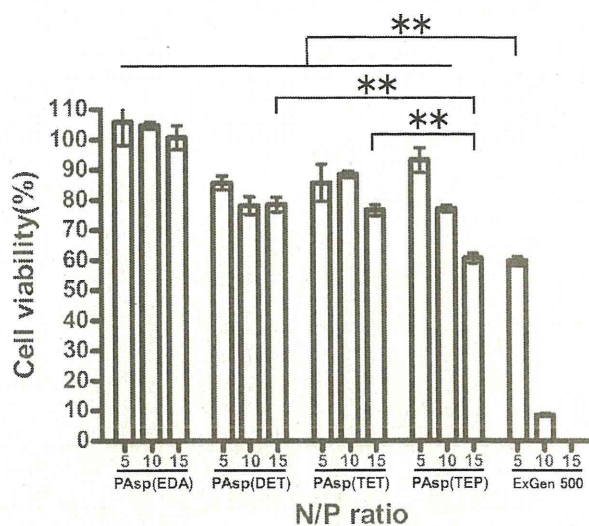


**Figure 6.** Cell viability assay of Huh-7 cells incubated with PAsp(EDA), PAsp(DET), PAsp(TET), PAsp(TEP), and ExGen 500 polyplexes under the same experimental conditions as in Figure 5. Results are expressed as mean ± SEM ($N = 4$). **$P < 0.01$.

constant ζ-potential of approximately 30 mV. Note that the formation of large aggregates around 1 $\mu$m was observed in each polyplex at a specific N/P ratio. Because each polyplex exhibited a ζ-potential close to neutral at this N/P ratio, large aggregate formation is expected to be due to decreased colloidal stability induced by charge neutralization. In the following experiments, the polyplexes prepared at N/P ratios above 4 were used because they apparently have similar physicochemical characteristics.

### In Vitro Transfection and Cytotoxicity.
The transfection efficiency of the luciferase gene in human hepatoma cells (Huh-7) was compared among the polyplexes prepared from PAsp(EDA), PAsp(DET), PAsp(TET), and PAsp(TEP) at N/P = 5, 10, and 15 (Figure 5). The polyplex from a linear PEI-based commercial transfection reagent (ExGen 500) was used as a control. Remarkable transfection efficiencies, which were higher than the maximum value obtained by ExGen 500 at N/P = 5, were achieved by polyplexes from PAsp(DET) (over N/P = 5) and PAsp(TEP) (over N/P = 10) possessing the even-numbered repeating aminoethylene units (PA-Es) ($P < 0.05$). Furthermore, polyplexes from PA-Es [PAsp(DET) and PAsp(TEP)] revealed significantly higher transfection efficiencies than those from PA-Os [PAsp(EDA) and PAsp(TET)] at all of the examined N/P ratios ($P < 0.01$). This remarkable odd−even effect on transfection efficiencies was not only limited to Huh-7 cells but was also observed for a human lung adenocarcinoma epithelial cells (A549) and a human umbilical vein endothelial cells (HUVEC) (Figure 3, Supporting Information). Note that a drastic reduction in the transfection efficiency was observed for the ExGen 500 polyplexes at higher N/P ratios, whereas it was not observed for any polyplexes from the N-substituted polyaspartamides. The substantially decreased transfection efficiency in the ExGen 500 polyplexes at higher N/P ratios is believed to be a direct result of severe cytotoxicity, as shown in Figure 6. In contrast, all polyplexes from the N-substituted polyaspartamides maintained a cell viability over 85% at N/P = 5 and over 75% even at N/P = 15, except for the polyplex from PAsp(TEP) at N/P = 15 (60%). Indeed, significant differences between the polyplexes from ExGen 500 at